Effects of Horizontal Grid Spacing and Inflow Environment on Forecasts of Cyclic Mesocyclogenesis in NSSL's Warn-on-Forecast System (WoFS)

KELSEY C. BRITT,[a,b,c] PATRICK S. SKINNER,[a,b,c] PAMELA L. HEINSELMAN,[c,b] AND KENT H. KNOPFMEIER[a,c]

[a] *Cooperative Institute for Mesoscale Meteorological Studies, University of Oklahoma, Norman, Oklahoma*
[b] *School of Meteorology, University of Oklahoma, Norman, Oklahoma*
[c] *National Severe Storms Laboratory, University of Oklahoma, Norman, Oklahoma*

(Manuscript received 15 June 2020, in final form 25 August 2020)

ABSTRACT: Cyclic mesocyclogenesis is the process by which a supercell produces multiple mesocyclones with similar life cycles. The frequency of cyclic mesocyclogenesis has been linked to tornado potential, with higher frequencies decreasing the potential for tornadogenesis. Thus, the ability to predict the presence and frequency of cycling in supercells may be beneficial to forecasters for assessing tornado potential. However, idealized simulations of cyclic mesocyclogenesis have found it to be highly sensitive to environmental and computational parameters. Thus, whether convective-allowing models can resolve and predict cycling has yet to be determined. This study tests the capability of a storm-scale, ensemble prediction system to resolve the cycling process and predict its frequency. Forecasts for three cyclic supercells occurring in May 2017 are generated by NSSL's Warn-on-Forecast System (WoFS) using 3- and 1-km grid spacing. Rare cases of cyclic-like processes were identified at 3 km, but cycling occurred more frequently at 1 km. WoFS predicted variation in cycling frequencies for the storms that were similar to observed variations in frequency. Object-based identification of mesocyclones was used to extract environmental parameters from a storm-relative inflow sector from each mesocyclone. Lower magnitudes of 0–1-km storm-relative helicity and significant tornado parameter are present for the two more frequently cycling supercells, and higher values are present for the case with the fewest cycles. These results provide initial evidence that high-resolution ensemble forecasts can potentially provide useful guidance on the likelihood and cycling frequency of cyclic supercells.

SIGNIFICANCE STATEMENT: The rate at which supercell thunderstorms produce rotating updrafts, known as cycling, can provide information on tornado potential. This study's purpose is to see if we can forecast the cycling rate of three supercells in an experimental model, called the Warn-on-Forecast System (WoFS). WoFS predicted higher cycling rates for supercells that cycled more frequently and lower cycling rates for supercells that cycled less frequently. These results provide a proof of concept that forecast models can potentially predict cycling frequency, which could be used to improve short-term forecasts of tornado likelihood. This is the first study examining the potential to predict cycling frequency in a forecast model; therefore, future work is needed to further analyze this potential using more case studies.

KEYWORDS: Mesocyclones; Severe storms; Supercells; Tornadoes; Ensembles; Numerical weather prediction/forecasting

1. Introduction

Cyclic supercells produce multiple mesocyclones with similar life cycles through a regenerative process known as cyclic mesocyclogenesis (Darkow and Roos 1970). These supercells have been commonly noted in observational (e.g., Lemon and Doswell 1979; Burgess et al. 1982; Dowell and Bluestein 2002a,b; Beck et al. 2006; French et al. 2008; Bluestein 2009; Kumjian et al. 2010; Houser et al. 2015) and numerical (e.g., Adlerman et al. 1999; Adlerman and Droegemeier 2002, hereafter AD02; Adlerman and Droegemeier 2005, hereafter AD05) studies. The mesocyclones produced by these supercells can have lifespans up to an hour or longer (Burgess et al. 1982), or as short as 6 min (Beck et al. 2006). Cyclic supercells that have slower cycling[1] frequencies tend to produce mesocyclones with longer durations that then have the potential to develop longer-track tornadoes. Rapidly cycling supercells may have a lower potential in generating destructive, long-track tornadoes owing to circulations occluding so quickly that tornadogenesis is hindered (Dowell and Bluestein 2002a,b; Beck et al. 2006; French et al. 2008). Thus, predicting the presence and cycling frequency of cyclic supercells may provide more specific guidance of severe thunderstorm threats to forecasters and the public by identifying which storms have the potential for long-track tornadoes and which do not.

The frequency at which supercells cycle is potentially dependent on the balance between the storm's inflow and outflow (Dowell and Bluestein 2002b; Beck et al. 2006; French et al. 2008). Dowell and Bluestein (2002b) found the balance between storm inflow and outflow plays a large part in whether cyclic storms will produce short- or long-lived mesocyclones and respective tornadoes. For instance, if the storm's low-level outflow is relatively weak compared to the inflow then the tornadoes moved rearward relative to the updraft, and decayed once they detached from the updraft. This flow imbalance

[1] "Cycling" is used as a short-hand for cyclic mesocyclogenesis throughout the rest of this paper.

Corresponding author: Kelsey Britt, kelsbritt@ou.edu

DOI: 10.1175/WAF-D-20-0094.1

resulted in relatively short-lived tornadoes. If the flow was balanced, the tornadoes remained under the updraft and in a region of strong convergence and upward acceleration to sustain themselves, allowing for longer durations.

The inflow/outflow balance affecting cycling frequency was also noticed by Beck et al. (2006) when analyzing a cyclic, nontornadic supercell. This supercell exhibited many similarities to previous studies of cyclic, tornadic supercells (Dowell and Bluestein 2002a,b), except it had a rapid cycling frequency (6 min). The authors hypothesized this was attributable to an imbalance between the storm's inflow and the rear-flank outflow (Dowell and Bluestein 2002b). The slow storm motion and broad westerly momentum on the southwestern side of the storm allowed for the rear-flank gust front (RFGF) to surge far ahead of each mesocyclone, leading to frequent cycling. Rapid displacement of the mesocyclones from the updraft likely contributed to tornadogenesis failure. French et al. (2008) also noted that when the inflow and rear-flank downdraft (RFD) outflow were balanced, the low-level mesocyclones could stay close to the RFGF and in an area of rich vorticity generation, increasing the potential for tornadogenesis. Thus, when the flow is balanced (unbalanced) then the cycling frequency is slow (rapid). Cyclic supercells with high cycling frequencies tend to produce more mesocyclones and short-lived tornadoes because the mesocyclones are shed at a faster rate. Supercells with slower cycling frequencies maintain their mesocyclones for a longer time, leading to an increased potential for producing long-lived tornadoes.

To the authors' knowledge, there have been no recent studies that have tried to forecast the potential or frequency of cycling in supercells. Adlerman et al. (1999) performed an idealized simulation of cyclic mesocyclogenesis, and later tested the sensitivity of cycling frequency to changes in horizontal grid spacing, microphysics schemes, and vertical grid spacing (AD02). They found cycling was dependent on horizontal grid spacing, with cyclic behavior ceasing at grid spacings coarser than 1 km. Later, AD05 tested environmental effects (e.g., hodograph shape, vertical wind shear magnitude and depth) on cycling. Cycling was found to have two modes: occluding cyclic mesocyclogenesis (OCM) and nonoccluding cyclic mesocyclogenesis (NOCM). OCM occurs when the RFGF surges ahead of the mesocyclone, encircles it, and forms an occlusion from the main updraft. The mesocyclone moves to the left of storm motion and decays in the supercell's heavy precipitation region. During NOCM, the mesocyclone travels south of the storm, down the gust front, and is essentially left behind by the storm while the second mesocyclone develops. The AD05 study found that cycling mode was sensitive to hodograph shape where quarter- and half-circle hodographs often resulted in OCM, straight-line hodographs were more likely to result in NOCM, and too much curvature of the hodographs can result in noncycling supercells. Also, cycling mode varied with values of storm-relative helicity (SRH). For instance, low values of SRH were often related to OCM, noncycling supercells had moderate SRH, and those exhibiting NOCM had the highest SRH values.

The AD02 and AD05 studies have yet to be revisited in a nonidealized framework. One way to gather information on forecasting cycling is through the use of quasi-operational, convection-allowing models (CAMs; $\Delta x \leq 4$ km) or ensemble prediction systems. However, the capability of convection-allowing prediction systems to potentially forecast cyclic mesocyclogenesis has not been explored. CAMs have been utilized by the Warn-on-Forecast (WoF) project, which strives to produce accurate, probablistic, short-range (0–6 h) forecasts for thunderstorm hazards (Stensrud et al. 2009, 2013). Experimental systems developed and tested by WoF project scientists have shown ability to produce accurate ensemble forecasts for severe convective events such as flash flooding (Yussouf et al. 2016), hail (Snook et al. 2016; Labriola et al. 2017), and tornadic mesocyclones (Dawson et al. 2012; Yussouf et al. 2013; Potvin and Wicker 2013; Wheatley et al. 2015; Yussouf et al. 2015). Recently, the real-time NSSL WoF System[2] (WoFS; Wheatley et al. 2015) has demonstrated skill in forecasting thunderstorms and mesocyclones (Wheatley et al. 2015; Yussouf et al. 2015; Jones et al. 2016; Skinner et al. 2016, 2018; Flora et al. 2019).

The purpose of this study is to test the capability of WoFS to resolve and predict cyclic mesocyclogenesis, assess whether this process is physically representative of the current understanding of cyclic supercells, and determine forecast performance of cycling frequency and presence. Four cyclic supercells are examined from three days in May 2017 that exhibited various cycling frequencies and mesocyclone totals (Table 1). To examine the impacts of changing horizontal grid spacing on the presence and frequency of cycling, WoFS 3-km forecasts are compared to forecasts run using a 1-km grid spacing. These forecasts are analyzed manually for evidence of cyclic mesocyclogenesis then compared to determine the impacts of grid spacing on cycling presence and frequency. Since AD02 found cycling terminated at grid spacings coarser than 1 km, we hypothesize that there will be no cycling in the 3-km forecasts, but will be observed in the 1-km forecasts. Next, differences in various storm-scale and environmental conditions within the supercells' inflow sectors are analyzed to identify how cycling frequency changes with the environment and compare those changes to changes found in AD05. From the AD05 study, we know that cycling can vary with environmental conditions, so we hypothesize that examining the inflow sectors for each storm will illustrate those dependencies.

The eventual goal of WoFS is to evolve from a CAM to a convection-resolving system. Determining the strengths and limitations of transitioning WoFS to a grid spacing of 1 km using its current configuration is the next step in that direction. Differences in how the four supercells evolve and cycle at 3- and 1-km horizontal grid spacing serves as a proof of concept study for the ability of a high-resolution CAM ensemble to provide specific predictions of supercell intensity and evolution.

Section 2 describes the data and methods used, and a brief background for each of the supercells analyzed. Changes in the presence and frequency of predicted cyclic mesocyclogenesis

[2] WoFS is formerly known as NSSL's Experimental WoF System for Ensembles (NEWS-e).

TABLE 1. Overview of supercell cases.

Date	Supercell	Start time (UTC)	End time (UTC)	No. of identified mesocyclones	No. of OCM cycles	No. of NOCM cycles	Total No. of cycles	No. of reported tornadoes
9–10 May 2017	Morton	2200	0548	7	6	0	6	1
16 May 2017	Elk City	2142	2328	3	1	1	2	6
18 May 2017	Corn	1846	2222	10	5	4	9	2
18 May 2017	Hennessey	2056	2328	5	4	0	4	0

in WoFS across different horizontal grid spacings and inflow environments are examined in section 3. Last, a summary of the results, the limitations of this study, and future work is provided in section 4.

2. Data and methods

a. *WSR-88D observation database*

To provide a verification dataset for the WoFS simulations, a radar observation database was created by analyzing Weather Surveillance Radar-1988 Doppler (WSR-88D) reflectivities and radial velocities for four supercells. The Level II radar data were attained from the National Centers for Environmental Information website (NCEI; www.ncdc.noaa.gov/nexradinv) and analyzed using the Gibson Ridge software (GR2Analyst). Since WoFS only assimilates radial velocity data out to 150 km in range from a radar site, only data within that radius of the closest radar to the supercell were examined (Table 2). One drawback of using WSR-88D data is the temporal frequency at which the radar produces volume scans, but this limitation was aided by the incorporation of Supplemental Adaptive Intravolume Low-Level Scan (SAILS). SAILS were available for all three of the case days and helped to reduce the low-level scan update interval by making the radar go back down to the base elevation angle (0.5°) once it has reached the middle of the atmosphere. This allowed for more scans of the low levels at shorter intervals (approximately 2 min), which is useful for viewing processes that occur very quickly (e.g., Heinselman et al. 2008; Heinselman and Torres 2011).

Radar reflectivities and radial velocities were manually analyzed to retrieve the maximum rotational velocity and diameter of the mesocyclones in a similar manner to the methods of Thompson et al. (2012, 2017) and Smith et al. (2012, 2013, 2015). Radial velocities were only included if they corresponded to an area of reflectivity $\geq$ 20 dBZ. Although GR2Analyst has a mesocyclone detection algorithm (MDA) built into the software, it did not reliably identify all mesocyclones; therefore, subjective analysis based on set criteria was needed for mesocyclone identification. Criteria for the classification of different rotation signatures in WSR-88D data were broken down into four categories (Table 3): mesocyclone, weak mesocyclone, tornado vortex signature (TVS), and/or vortex signature (VS). The WSR-88D circulations may be given more than one classification. The criteria for the rotational velocities and mesocyclone diameters were chosen based on past research (Dowell and Bluestein 2002a,b; Beck et al. 2006; French et al. 2008; Thompson et al. 2012, 2017; Smith et al. 2012, 2013, 2015), and by considering the spatial and temporal limitations of the WSR-88D radar data.

The "weak mesocyclone" criterion (Table 3) was created for cases when a clear circulation was present in the radial velocities, but the circulation's rotational velocity was slightly below the threshold to be considered a mesocyclone. Since the rotational velocity threshold of 20 m s^{-1} was adopted by many studies that used mobile Doppler radar data (Beck et al. 2006; French et al. 2008), this extra classification accounts for the loss of information or the greater uncertainty caused by the lower temporal and spatial resolutions of WSR-88D radar data. Additionally, there were multiple times when a mesocyclone had strengthened and tightened enough to be also considered either a TVS or VS. A circulation was considered to be a VS if it had a rotational velocity $\geq$ 20 m s^{-1}, a diameter no greater than 2 km, and no tornado reports at the time and location that the signature occurred (French et al. 2013). A TVS has the same criteria except the circulation has a corresponding tornado report within 10 min and in the same location that the TVS occurred (French et al. 2013). Depending on the diameters of the TVS or VS, it may also be labeled as a mesocyclone.

b. *Supercell cases*

Four cyclic supercells were chosen from three severe weather days in May 2017 to examine the effects of horizontal grid spacing and inflow environment on cyclic mesocyclogenesis (Fig. 1, Table 1). The first case was the 9–10 May 2017 Morton supercell, which initiated (reflectivities $\geq$ 30 dBZ) in far-eastern

TABLE 2. Radar information for the four cyclic supercell cases.

Case date	Supercell name	Radar site(s) used	Tilt of radar beam (°)	Volume coverage pattern(s)
9 May 2017	Morton	KLBB	0.445	12 212
16 May 2017	Elk City	KFDR	0.396	212
18 May 2017	Corn	KFDR, KTLX	0.396	212
18 May 2017	Hennessey	KFDR, KTLX	0.53	212

TABLE 3. Circulation criteria (V_{rot} is rotational velocity).

Classification	Rotational velocity ($m\,s^{-1}$)	Diameter (km)	Other criteria
Mesocyclone	≥20	1–10	Continuous in time; must be present for at least two consecutive volume scans
Weak mesocyclone	$15 \leq V_{rot} < 20$	1–10	Continuous in time; must be present for at least two consecutive volume scans
TVS	≥20	<2	Must be associated with tornado report
VS	≥20	<2	No tornado report

NM and decayed in the central Texas Panhandle (Table 1). This storm took a couple hours to mature before producing a mesocyclone around 0133 UTC (10 May 2017) over Gladiola, Texas. A total of six cycles and seven mesocyclones were observed in WSR-88D data for the supercell (Fig. 2). The main mode of cycling was OCM. The occlusion process can be seen in the tracks for the first five mesocyclones, which have the characteristic left turn toward the end of the track (the sixth mesocyclone was short-lived and did not exhibit a turn; Fig. 2). The mesocyclone turning to the left of storm motion signals the occlusion of the mesocyclone from the main updraft, and being swept into the storm's heavy precipitation region (e.g., Burgess et al. 1982; Dowell and Bluestein 2002b; AD02). Once the mesocyclone is surrounded by this negatively buoyant air it begins to decay, and the track ends.

The second case was the 16 May 2017 Elk City supercell (Table 1). This storm initiated at approximately 2142 UTC in the western Texas Panhandle. The cell developed its first mesocyclone at 2229 UTC, then decayed around 0106 UTC (17 May 2017) in western Oklahoma. The Elk City supercell produced five tornadoes, the most of the cases examined in this study (Table 1). The majority of the tornadoes were weak and rated EF0; however, this storm did produce one long-track EF2 tornado, which caused extensive damage in and around Elk City, Oklahoma. This supercell exhibits both modes of cyclic mesocyclogenesis with NOCM occurring during the first cycle (Fig. 3), and OCM occurring for the subsequent mesocyclones (Fig. 4).

The final two cases occurred on 18 May 2017 and were nicknamed the Corn and Hennessey supercells, respectively (Table 1). The Corn supercell initiated in southwest Oklahoma and decayed in west-central Oklahoma. This cell was responsible for producing two EF0 tornadoes, one near East Duke, Oklahoma, and another near Corn, Oklahoma. This storm is similar to that of the Elk City supercell in that it exhibited both modes of cycling (Fig. 2). The first four mesocyclones identified for this storm go through NOCM, while the remaining five mesocyclones all go through OCM (Fig. 2). Unfortunately, the nonoccluding cycles and much of the Corn storm lifespan occurred prior to the WoFS forecast initialization. The Hennessey supercell formed on the rear flank of the Corn storm and merged with it before decaying (Fig. 1). The Hennessey cell had a total of five mesocyclones identified in WSR-88D data, which all went through OCM. Unlike the Corn supercell, the entirety of the Hennessey supercell duration was covered by WoFS forecasts. The Corn and Hennessey supercells were analyzed together because they were both cyclic, provided a longer period of cyclic behavior to examine, and were close enough together to dynamically influence one another. For instance, when the storms merged, the Hennessey storm may have rained into the rear flank of the Corn storm causing the RFD of the Corn cell to intensify and occlude the mesocyclone (Hastings and Richardson 2016).

c. *WoFS specifications*

WoFS is an ensemble data assimilation and prediction system nested within the experimental High-Resolution Rapid Refresh Ensemble (HRRRE; Dowell et al. 2016) run by the National Oceanic and Atmospheric Administration/Earth System Research Laboratory (NOAA/ESRL). The 2017 WoFS configuration consisted of 36 ensemble members with the Advanced Research Weather Research and Forecasting dynamic core (WRF-ARW; Skamarock et al. 2008; Powers et al. 2017). WoFS used an ensemble Kalman filter (EnKF; Anderson and Collins 2007) to produce analyses every 15 min by assimilating WSR-88D radial velocities and reflectivities (Wheatley et al. 2015), surface observations from the Oklahoma Mesonet (when applicable), and satellite cloud total liquid water path (Jones et al. 2016). This system then produced real-time, short-term, probabilistic forecasts from 1900 to 0300 UTC on the day of the event. WoFS utilized the Rapid Radiative Transfer Model (RRTM) shortwave radiation scheme and the Rapid Radiative Transfer Model for GCMs (RRTMG) longwave and shortwave parameterization schemes (Wheatley et al. 2015, their Table 2). WoFS also uses diverse planetary boundary layer

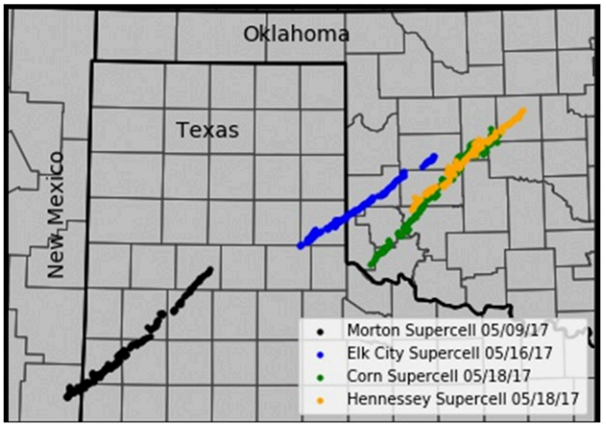

FIG. 1. Overview of all mesocyclones identified associated with the four supercell cases that were analyzed.

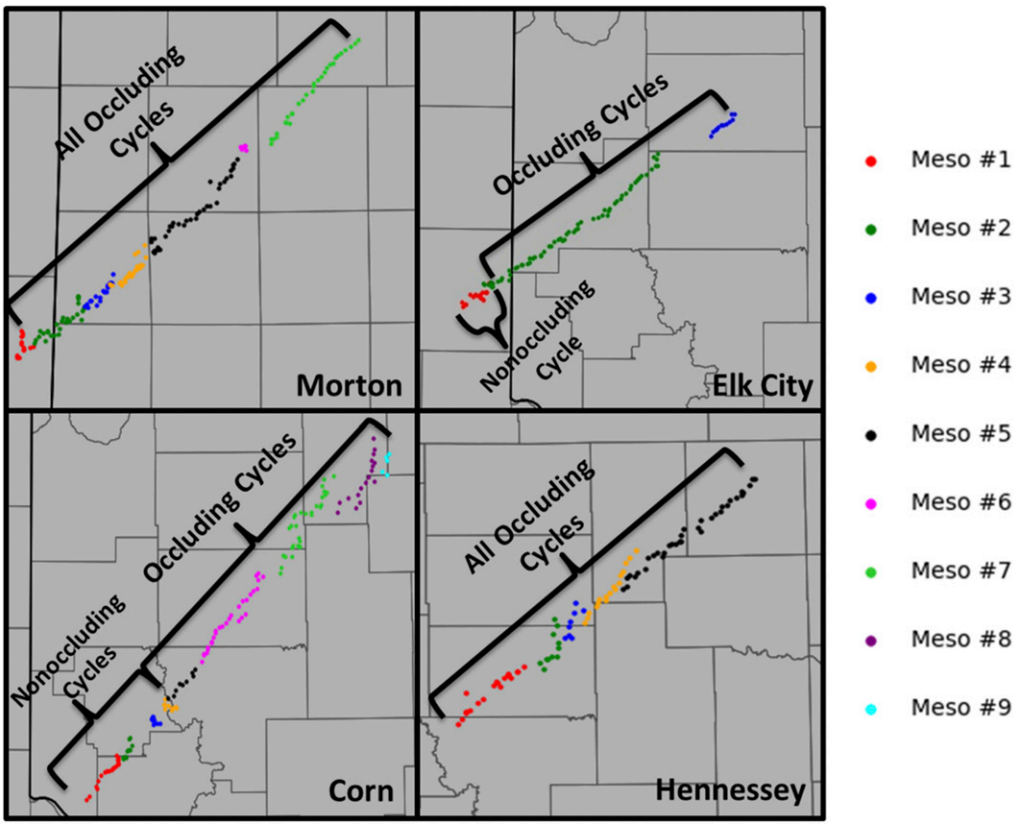

FIG. 2. Color-coded mesocyclones for the four supercells: Morton, Elk City, Corn, and Hennessey. The brackets indicate the type of cycling that occurred between the mesocyclones (occluding or nonoccluding cyclic mesocyclogenesis).

(PBL) parameterizations, including the Yonsei University (YSU), Mellor–Yamada–Janjić (MYJ), and the Mellor–Yamada–Nakanishi–Niino (MYNN) schemes (Wheatley et al. 2015, their Table 2). However, all ensemble members use the NSSL two-moment microphysics scheme (Mansell et al. 2010). WoFS was run over a $750 \times 750\ km^2$ grid with a 3-km horizontal grid spacing. A full list of the physical and computational WoFS parameters are shown in Table 4. For a more comprehensive background on the specifications and configuration of WoFS, the reader is directed to Wheatley et al. (2015).

The HRRRE provides the boundary and initial conditions used to initialize the WoFS analyses at 1800 UTC daily. The location of the WoFS 3-km domain varies from case to case, and is determined based on the Storm Prediction Center's (SPC) Day 1 Convective Outlook. The domain is then placed over the region most favorable for the development of severe convection. Ensemble analyses are produced every 15 min using the EnKF technique provided by the Data Assimilation Research Testbed (DART; Anderson and Collins 2007; Anderson et al. 2009). The 18-member forecasts are issued every half-hour beginning at 1900 UTC and ending at 0300 UTC. The duration of the forecasts is 180 or 90 min, depending on whether the forecast was issued at the top or the bottom of each hour, respectively. The 90-min forecasts are not considered in this study as there is insufficient time to identify cyclic mesocyclogenesis.

In this study, only the last 2 h of the 3-h forecasts are considered because the first hour of each forecast contains excessive spurious echoes attributable to imbalances introduced by data assimilation. The cutoff time of an hour was chosen from results of previous research from Skinner et al. (2018; their Fig. 5), who found an overprediction bias in thunderstorm objects across 18 WoFS cases from 2017 that was maximized in the first hour of forecast lead time. Following the first forecast hour, the frequency bias of the storm objects decreases to nearly 1, indicating an unbiased forecast for the 1–3-h period of lead time (Skinner et al. 2018).

d. WoFS grid-spacing sensitivity

The first part of this study consists of running WoFS forecasts at a finer horizontal grid spacing of 1 km to test the forecasts' sensitivity to grid spacing. The n-down (also known as nest-down; Skamarock 2004) technique was used to create all of the 1-km forecasts. This process takes the same initial conditions as the 3-km forecast and interpolates them onto a 1-km grid. This method allows for the changes in forecasts related to horizontal grid spacing to be isolated from other potential changes in the forecast as the two forecasts will have similar initial conditions. The domain size for the 1-km grid is

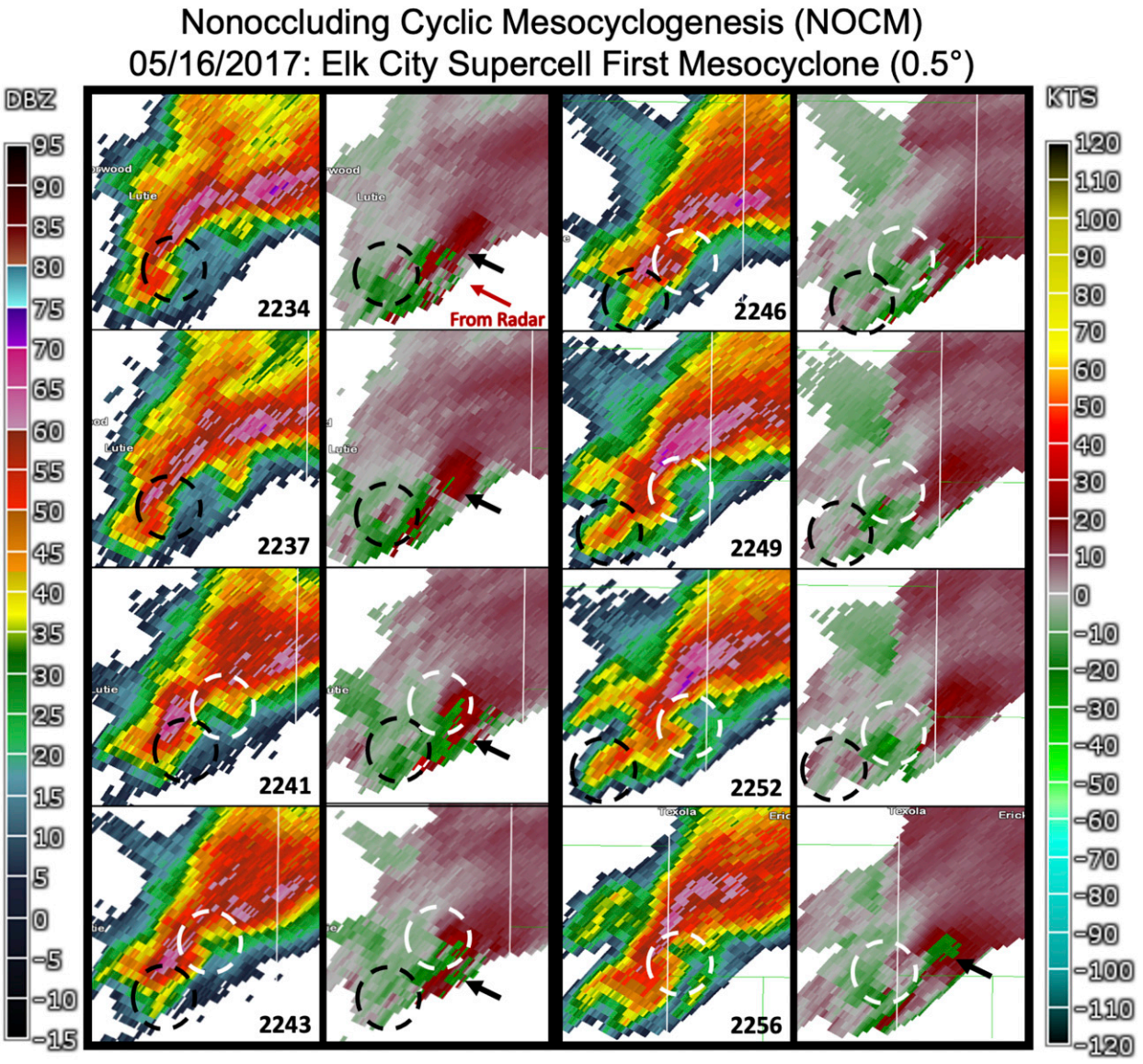

FIG. 3. Nonoccluding cyclic mesocyclogenesis of the first mesocyclone in the Elk City supercell of 16 May 2017. (left) Reflectivities and (right) radial velocities are taken from KFDR at the lowest elevation angle (0.5°). Time is given in UTC at the bottom right of each panel. The dotted, black circles indicate the first mesocyclone, while the dotted, white circles represent the second mesocyclone. The black arrows point at persistent sidelobe contamination and dealiasing problems to the east of the mesocyclones. The red arrow is pointing from the location of the KFDR radar site.

approximately 350 × 350 km^2 and is positioned so that the track of the supercell of interest in centered within the high-resolution domain (Fig. 5). Placing the supercell track in the center of the domain helps to mitigate the impacts of the boundary conditions at longer forecast times.

e. WoFS inflow environments

The second part of this study compares the supercells' inflow environments to examine how environmental conditions may have affected cyclic mesocyclogenesis in the WoFS forecasts. To highlight main environmental differences between the supercells, composites of the storm environments are created by using object identification (Skinner et al. 2018) to extract the near-storm and storm-scale parameters. The object-based framework allows for the stacking of environments taken from a similar storm-relative area in different member forecasts.

The first step in creating composites of WoFS predictions of the inflow environments is to isolate the tracks of the supercells of interest in the WoFS domain. The 2-h, 0–2-km layer updraft helicity (UH) swaths are plotted across the full WoFS domain for each ensemble member. Manual analysis was used to identify the swath belonging to the storm of interest for all ensemble members. The goal of the manual analysis was to ensure that the correct swath object was chosen, combine

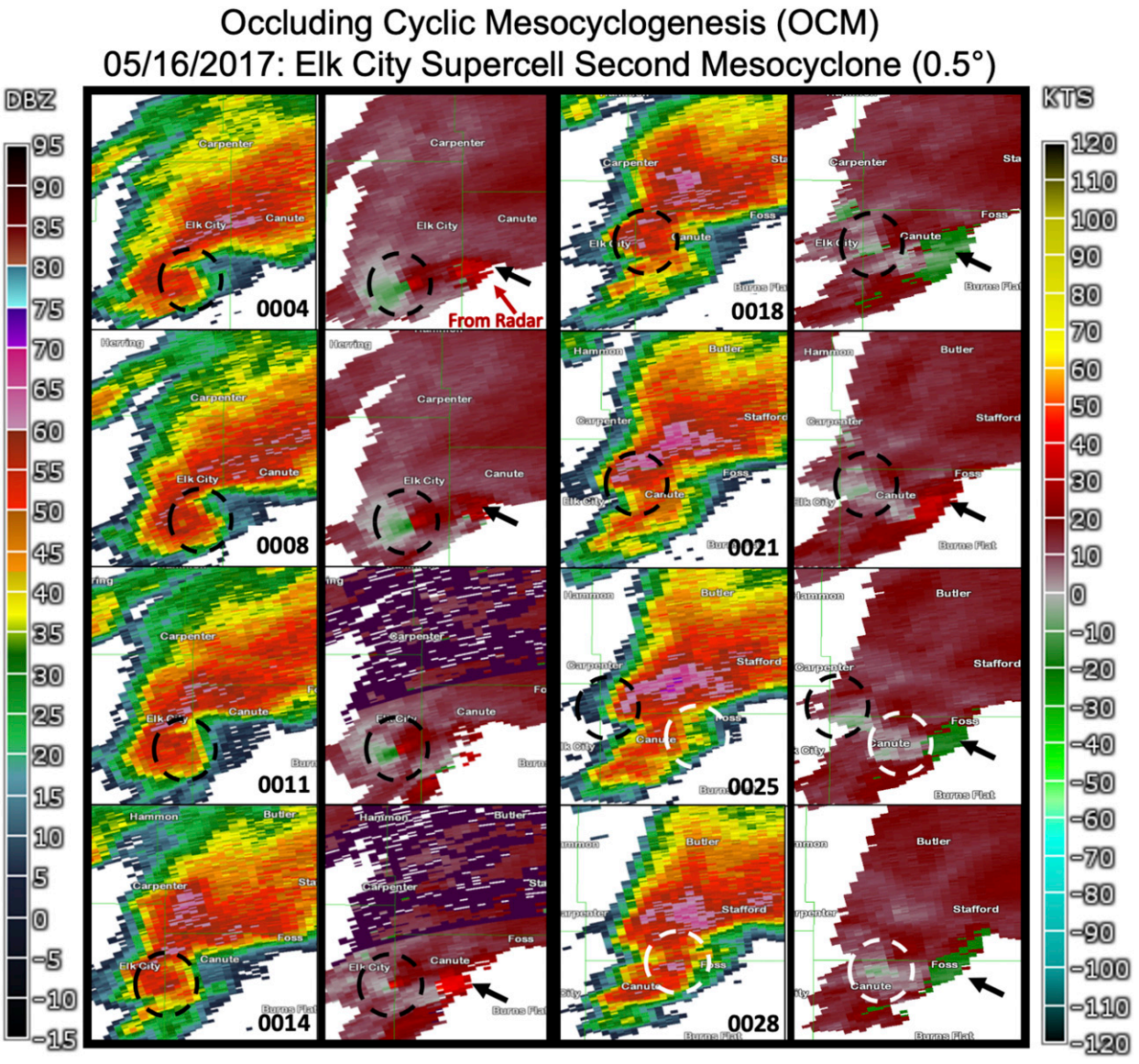

FIG. 4. Occluding cyclic mesocyclogenesis of the second mesocyclone in the Elk City supercell of 16 May 2017. As in Fig. 3, but the black circle indicates the second mesocyclone, and the white circle shows the third mesocyclone.

pieces of the swath object if it was discontinuous, and eliminate all other swaths from the WoFS domain. UH 0–2-km thresholds were utilized to condense the number of storms present in the domain. Those thresholds were on average $20\,m^2\,s^{-2}$ for the 3-km forecasts and $30\,m^2\,s^{-2}$ for the 1-km forecasts. Gaussian smoothing was applied to the 1-km forecasts to improve the continuity of UH swath objects, which tend to be more discontinuous at higher resolutions.

Once the full 2-h, UH 0–2-km swaths were identified, the inflow environments could be extracted every 30 min for each WoFS forecast. The inflow environment is defined as a 150° sector from the Bunkers's storm motion vector (Bunkers et al. 2000) extending to a radius of 80 km from the object centroid (e.g., the center of the supercell's mesocyclone; Fig. 6). The sector was chosen to be 150° so that it included a substantial portion of the storm's inflow, but not the outflow. The Bunkers's storm motion vector was averaged for all included samples to ensure that the sectors were aligned. The resulting composites for a single WoFS forecast are an average of all inflow environments extracted every 30 min through that 2-h forecast for all ensemble members with the storm present. If at any point an inflow sector extended beyond a domain boundary, which rarely occurred for storms dissipating on the edge of the domain, the sector would be ignored.

3. Results

a. *Effects of changing horizontal grid spacing*

The AD02 idealized simulations found resolving cyclic mesocyclogenesis to be sensitive to changes in horizontal grid

TABLE 4. System configuration and physical parameterizations for WoFS.

Parameter	Value/description
Horizontal grid resolution	3 km
3-km grid domain size	750×750 km^2
Location of grid	Event specific
1-km grid domain size	Approximately 350×350 km^2
No. of vertical levels	51
Vertical grid resolution	100 m at surface and 1 km at top (10 hPa)
Grid points	$251 \times 251 \times 50$
Microphysics scheme (all members)	NSSL two-moment scheme
PBL schemes	YSU, MYJ, MYNN
Radiation (shortwave/longwave)	Dudhia/RRTM, RRTMG/RRTMG
Land surface	RAP land surface model
Total No. of ensemble members	36
No. of ensemble forecast members	18

spacing, where cycling terminated at grid spacings coarser than 1 km. This result exposes a likely limitation of operational and experimental CAMs using a grid spacing of 3 km. To examine the impact of horizontal grid spacing on WoFS' ability to resolve cycling, the 3-km forecasts were interpolated to a 1-km grid and rerun. We hypothesized that there would be no evidence of cycling in the 3-km WoFS forecasts, but cycling would be observed in the 1-km forecasts, as in AD02.

The majority of the 3-km WoFS forecasts did not show any evidence of cyclic mesocyclogenesis. However, there were a total of seven cases in which "cyclic-like" mesocyclogenesis was identified in 3-km forecasts: two in the Corn supercell and five in the Hennessey supercell. The cycling process examined in the 3-km WoFS forecasts is termed "cyclic-like" as they behave similarly to cycling observed by radar, but occur at grid resolutions that are too coarse to fully resolve them.

One case of 3-km cyclic-like mesocyclogenesis was simulated by WoFS ensemble member 2 for the Hennessey supercell (Fig. 7). The supercell's first mesocyclone is observed from 2250 to 2345 UTC. The mesocyclone is represented by an area of high vertical velocities and corresponding maximum vertical vorticities (Fig. 7). Following 20–25 min, the mesocyclone starts to occlude from the updraft and move to the left of the storm motion, where it becomes embedded in the downdraft and precipitation zone of the supercell (represented as negative vertical velocities in Fig. 7). At 30 min, a second mesocyclone forms at the apex of the gust front corresponding to the swath of positive vertical velocities on the southeast periphery of the supercell. As the second mesocyclone matures, the first mesocyclone decays in the supercell's heavy precipitation region. The above process is similar to those outlined in previous numerical (Adlerman et al. 1999) and observational (Burgess et al. 1982; Beck et al. 2006; French et al. 2008) studies. The remaining cases of 3-km cyclic-like mesocyclogenesis that occurred with the Hennessey and Corn supercells exhibited similar characteristics to those seen in Fig. 7 (not shown).

An unexpected result of this study was the evidence of cyclic-like mesocyclogenesis occurring in simulations with 3-km grid spacings, which was contrary to the findings from AD02. However, their numerical study was an idealized simulation with no PBL or radiation parameterizations, and was

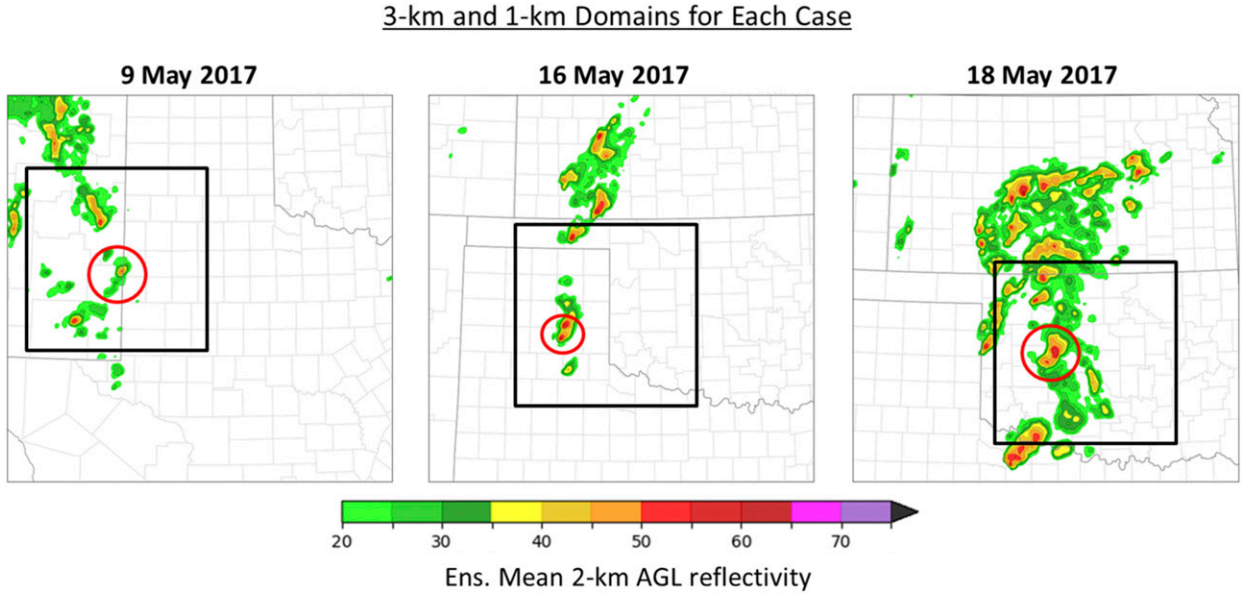

FIG. 5. Domains for the 3- and 1-km WoFS grids for all three cases. The full domain corresponds to the 3-km grid and the black square indicates the 1-km domain region, which is centered around the full track of the supercell not just the supercell at a given time. The red circles highlight the supercells of interest to illustrate their locations within the WoFS domains. Images for 9, 16, and 18 May 2017 were taken at the beginning of the 2300, 2100, and 2200 UTC forecasts, respectively. The domains remain constant for all forecast times.

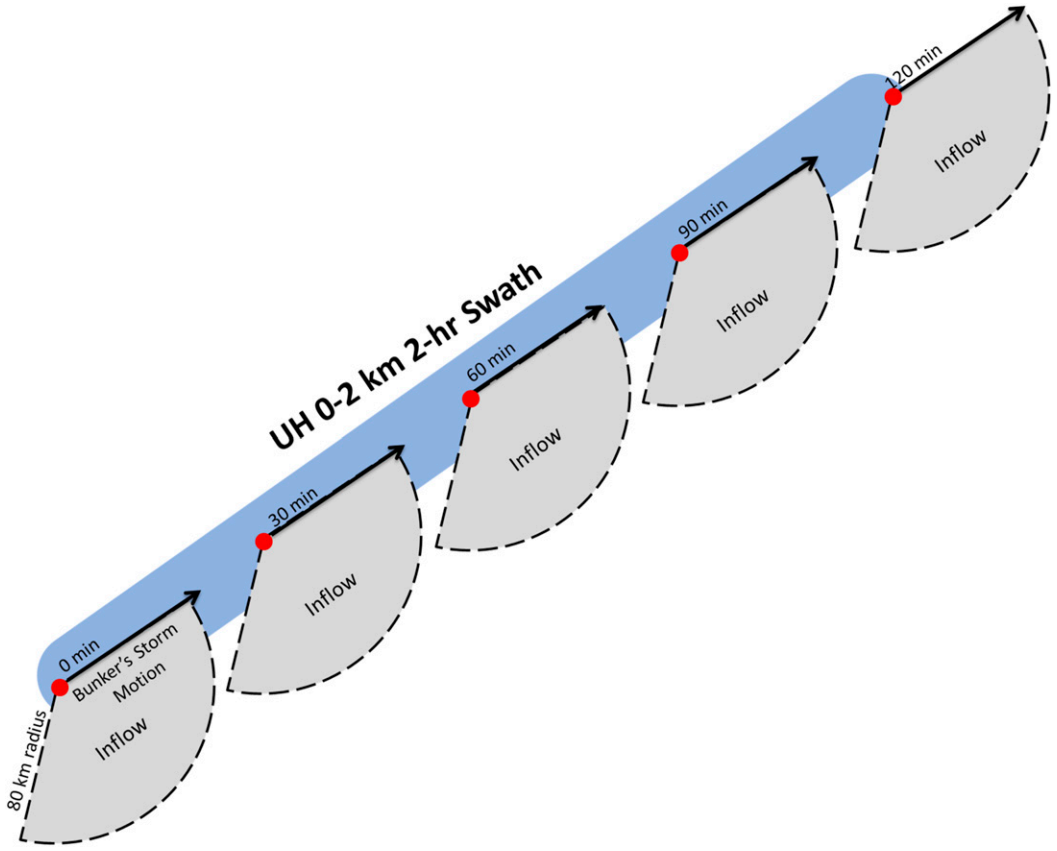

FIG. 6. Schematic to illustrate the inflow sector identification method that is used to extract environmental variables from each mesocyclone object. The 2-h forecast environments are sampled every 30 min. The blue track represents the UH 0–2-km swath and the red dots are the mesocyclone objects at each time stamp. The black arrows indicate the direction of the mean Bunkers storm motion vector, calculated by taking the mean of all the ensemble Bunkers vectors for each forecast. A 150° sector bounded on the left by the Bunkers motion with a radius of 80 km is taken from each object centroid to represent the inflow environment of the storm. Only the data within these sectors are extracted for composites.

horizontally homogeneous in nature. WoFS utilizes multiphysical parameterizations for PBL, longwave, and shortwave radiation. Additionally, the AD02 study used the Kessler warm rain microphysical scheme for their control simulation, which only consists of rain. They found adding ice microphysics to the model tended to better resolve cycling. WoFS utilizes the NSSL two-moment microphysical scheme, which has six hydrometeor species and is often used for real-time forecast systems. Therefore, the physical variations in WoFS that were not included in the original AD02 study may have helped the system predict the possibility of cyclic-like mesocyclogenesis processes at 3 km.

Understanding the limitation that running WoFS at 3 km would likely not produce cases of cycling, 1-km forecasts were generated to analyze the differences in cycling between grid spacings, forecast member, and case date. As expected, cyclic mesocyclogenesis was present and more frequent in the WoFS forecasts run with a horizontal grid spacing of 1 km than 3 km (AD02). One example of the differences that are observed in the 3-km WoFS forecasts versus the 1-km forecasts is that of the WoFS 2100 UTC, ensemble member 2 forecast of the Hennessey supercell. For this specific forecast, cycling was present on both the 3-km (Fig. 7) and the 1-km grids (Fig. 8). Note that the time period for cycling at 1 km is displaced 15 min from that at 3 km. This was the closest example to observing roughly the same cycling process at different grid spacings.

For the 1-km forecast, the Hennessey supercell and its mesocyclones are simulated with more detail than that at 3 km. At 3 km, the supercell only had one occluding cycle (Fig. 7), but at 1 km, the supercell has two occluding cycles over the same time period that follow the same cycling process as seen at 3 km. These cycling episodes are simulated over 2235–2330 UTC (Fig. 8). Following 10–15 min into the 1-km forecast, the first mesocyclone starts to turn toward the rear of the storm as it becomes surrounded by downdraft air (Fig. 8). At 25 min, a second mesocyclone forms at the bulge of the gust front as the first mesocyclone decays in the supercell's heavy precipitation region. The second cycle starts around 35 min when the downdraft starts to impinge on the second mesocyclone. At 40 min, the mesocyclone is completely surrounded by downdraft air. Last, the third mesocyclone forms 15 min later.

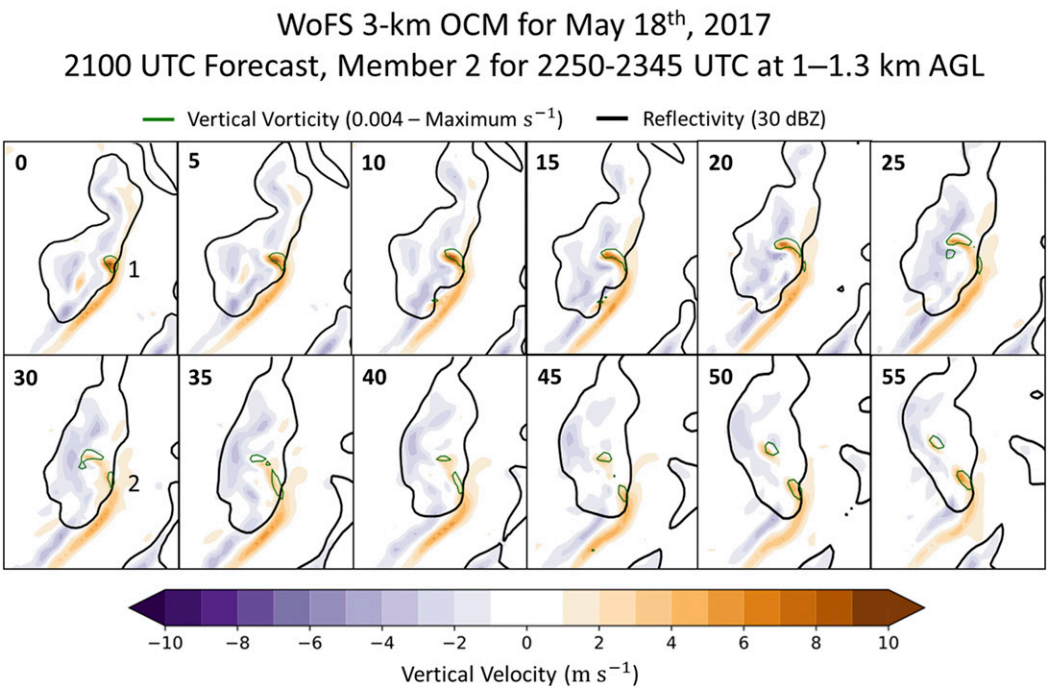

FIG. 7. Occluding cyclic mesocyclogenesis seen in WoFS member 2 at 3 km during the 2100 UTC (2250–2345 UTC) forecast on 18 May 2017 for the Hennessey supercell. Maximum vertical vorticity is contoured in green, vertical velocities are colored, and the black outline represents the 30-dBZ reflectivity line. The time is shown in the upper left corner of each panel and is in minutes after the start time (2250 UTC). Mesocyclones are numbered as they first appear.

In 1-km forecasts, supercell cases that had a greater number of observed cycles, such as the Morton and Hennessey supercells, exhibited an overall higher number of forecasted cycles and higher cycling frequencies in WoFS (Fig. 9). Cycling frequency is given as cycles per hour to quantify the differences between the number of cycles produced by each storm in the WoFS forecasts. In the past, cycling frequency was quantified by using the average mesocyclone duration for a storm. However, this was not applicable for the current study because of the short forecast times (2 h) resulting in many forecasts where a single episode of cycling occurred. Therefore, the total number of forecasted cycles is found by counting all the cycles that occurred over different forecast times and ensemble members. The Elk City supercell only had three observed cycles, which corresponded with a lower frequency of predicted cycling occurrences in WoFS. Elk City also had the lowest number of cycles across all four of its forecasts compared to the Morton and Hennessey supercells (Fig. 9a). Since the supercells can be categorized by cycling frequency, the Hennessey and Morton supercells will hereafter be referred to as frequently cycling supercells, whereas the Elk City supercell is an example of an infrequently cycling supercell.

The Morton supercell produced seven identified mesocyclones in WSR-88D data with six cases of OCM (Fig. 2). In the 1-km WoFS forecasts, a total of 32 cycles were simulated (Fig. 10). The forecast times examined for this case exhibited both cycling types, even though NOCM was not observed on radar during this supercell. Similarly, predictions of the Hennessey case also underwent frequent cyclic mesocyclogenesis. This supercell had 42 forecasted cycles in WoFS (Fig. 11), which was the highest number of forecasted cycles out of all cases. The observed Hennessey supercell produced five identified mesocyclones and exhibited four periods of OCM on WSR-88D radar (Fig. 2). All of the cycles forecasted in WoFS were also OCM.

The Elk City supercell is an example of an infrequently cycling supercell because only two observed cycles were identified on radar (Fig. 2). The 1-km WoFS ensemble members forecasted a total of 19 cycles for this supercell (Fig. 12). The first observed cycle for this supercell was characterized by NOCM. However, in the WoFS forecasts, there was only one case of NOCM forecasted (i.e., member 4 during the 2200 UTC forecast in Fig. 12). Also, compared to the Morton and Hennessey supercells, the first cycles predicted for the Elk City supercell began relatively late into the forecast period (Fig. 12). This supercell took longer to cycle and the cycles that did occur had longer durations than those forecasted for the other supercells.

Last, the Corn supercell only exhibited two cases of OCM (not shown). The first WoFS forecast considered by this study is initialized at 2000 UTC, 2 h after the Corn Storm formed. Additionally, the first hour of the 2000 UTC forecast is not used, so the first available WoFS forecast times are at 2100 UTC. By this time, the Corn storm was dissipating and WoFS generally predicted it to dissipate as well. Therefore, a sufficient sample of Corn's mature phase is not available in

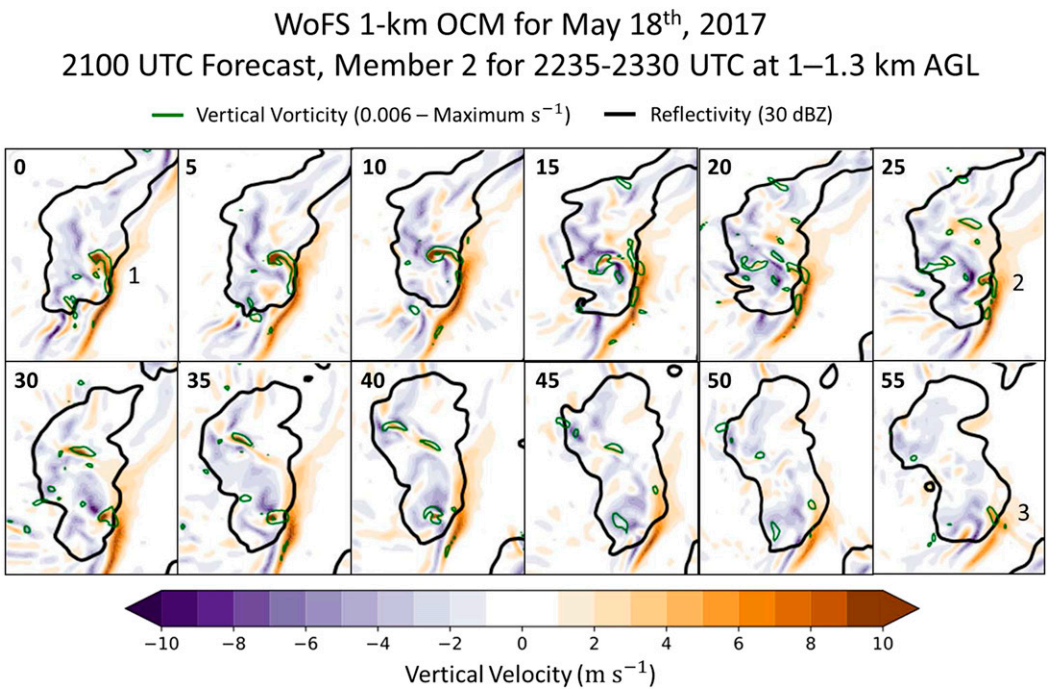

FIG. 8. As in Fig. 7, but at 1 km. Note that these images are for a slightly different time frame than that in Fig. 7 (2235–2330 UTC).

WoFS guidance to meaningfully compare observed and predicted cycling frequencies. Due to this limitation, the Corn supercell will not be included in the rest of the analysis.

WoFS predicted variation in cycling frequency that matched variation in the observed cycling frequency for each supercell. In observations, the two frequently cycling cases were the Morton and Hennessey supercells. In these cases, the forecasted cycling frequencies tended to be higher, and these storms had a larger percentage of forecasts that cycled over those that did not (Fig. 9b). Elk City, on the other hand, was an infrequently cycling supercell in observations. WoFS forecasted a lower cycling frequency, and this storm had a smaller percentage of cycling forecasts, which meant more forecasts did not simulate any cycling compared to those that did (Fig. 9b). WoFS shows potential for predicting the relative rates of cycling frequency (i.e., discriminating between frequently cycling and infrequently cycling supercells) in this small dataset, but the forecasted cycling frequencies are lower than the observed for all three cases. Therefore, WoFS is not accurately predicting the observed cycling rates for these storms. However, AD02 found that cycling increases as resolution is increased, so a 1-km grid spacing may still underpredict observed cycling frequency as cyclic mesocyclogenesis is insufficiently resolved.

Another difference between the WoFS forecasts of the three supercells is the timing at which the first cycle begins. For the Elk City supercell, the first cycle occurs an average of 70–88 min into the forecast (excluding the first hour of the forecast; Fig. 12). The storm takes a long time to produce its first cycle, which inhibits its ability to produce many more cycles before the forecast is over. On the other hand, the Hennessey and Morton supercells are relatively quick in producing their first cycle averaging 54–59 min and 25–68 min, respectively (Figs. 11 and 10). Morton exhibits more variability in its timing than the other two storms, attributable to the second forecast taking longer (68 min) than the first and third forecasts.

Comparisons of the three supercells provide preliminary evidence that WoFS may be able to forecast the relative cycling frequency of supercells. Predictions of any one cycle are inaccurate and the overall cycling frequency will likely be underpredicted. However, it may be possible to predict relative cycling frequencies in different supercells, which is potentially important for tornado prediction. For instance, supercells with higher cycling frequencies tend to produce fewer tornadoes as mesocyclones are shed too quickly for tornadogenesis, or if they do produce tornadoes, they would be weak and short lived. On the other hand, a supercell that has a lower cycling frequency, or may not cycle at all, tend to have a higher potential for producing long-lived tornadoes.

To further examine differences in WoFS predicted frequency of cycling, inflow sectors are compared for each of the mesocyclones produced by these storms. Environmental conditions within these inflow sectors may shed some light on why WoFS predicts variable cycling frequencies and whether the variation is consistent with physical processes characteristic of cyclic supercells (AD05).

b. *Inflow environments*

Analysis of the 1-km forecasts suggest that WoFS can potentially provide guidance on supercell cycling frequency. AD05 found differences between environmental parameters could affect the supercell's cycling mode (i.e., occluding,

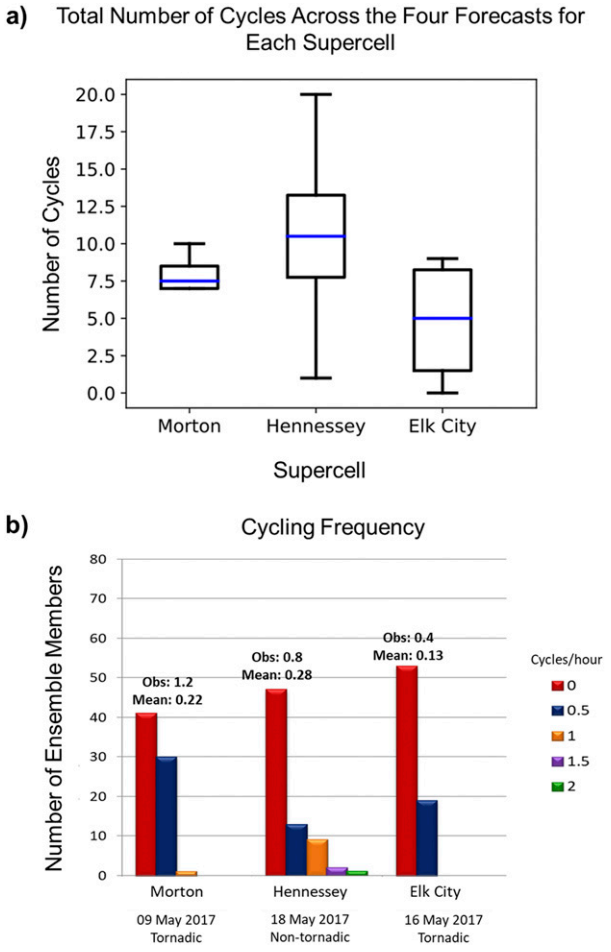

FIG. 9. (a) Box-and-whisker plots showing the summation of cycles over each of the four forecasts for each storm. The whiskers denote the range of the data and the blue line is the median. (b) Cycling frequency for the four supercells at 1 km. The bars denote the cycles per hour observed with each supercell. The observation value and the mean above the bars represent the cycles per hour in the observations and the mean of the distribution for each supercell, respectively.

nonoccluding, or steady-state), so an analysis of the environment for each supercell predicted by WoFS is undertaken. Composites of the inflow environments of the three supercells are created to intercompare bulk differences between their respective mesoscale environments.

First, composite hodographs for each supercell are analyzed to examine differences between their respective hodograph shape and relative inflow strength. The hodographs were calculated at a series of points to the southeast of the mesocyclone center every 20 km from the centroid (Fig. 13). To avoid regions of storm modification and get the best representation of the far-inflow region (Parker 2014), only the 40–80-km points were considered. However, for each individual supercell, the shape and magnitude of their hodographs from 60 to 80 km were similar to those at 40 km. Therefore, only the 40-km hodographs for each respective storm are shown (Fig. 14).

The shape of the hodographs for the Morton and Hennessey supercells are closest to quarter-circle with most of the shear concentrated in the lowest 1 km (Fig. 14). The early forecast hodographs for Elk City are quarter-circle, but the later forecasts move toward a more half-circle hodograph shape with the largest shear occurring throughout the lowest 6-km layer. The evolution of the Elk City hodographs occurs coincident with the evening boundary layer transition and is a good example of how development of the low-level jet (LLJ) can influence the hodograph's curvature (Fig. 14). The LLJ typically develops around 0100–0300 UTC, and helps to destabilize the environment, increase low-level shear, and enhance low-level convergence and associated vertical motion (Mead and Thompson 2011). Additionally, the Hennessey supercell was also influenced by the LLJ, but one with an easterly wind component that elongated the forecasted hodographs (Fig. 14). Last, the forecasts of the Morton supercell occurred after the LLJ developed and, thus, is why the hodographs for this storm are relatively constant with forecast time.

Comparing the shape of the Morton, Elk City, and Hennessey forecasted hodographs to those seen in AD05 (their Fig. 21), the WoFS composite hodographs would be expected to exhibit primarily NOCM, with the later forecasts of the Elk City primarily steady-state (i.e., noncycling). However, the prominent cycling mode for these storms was OCM. This discrepancy between cycling mode in WoFS hodographs and expectations based on AD05 is not entirely surprising given the large model configuration difference between WoFS and the idealized simulations of AD05. Also, AD05 only changed the kinematic properties of their inflow soundings, so their hodographs do not capture the influence of variation in other environmental parameters that may affect cycling. However, one similarity between the AD05 and this study is that the inflow environment does seem to be influencing cycling frequency in a systematic manner.

In AD05, one of the environmental parameters that modulated the frequency of cycling was storm-relative helicity from 0 to 1 km (hereafter SRH01). They found that SRH01 was lower than $200\,m^2\,s^{-2}$ for OCM, between 0 and $550\,m^2\,s^{-2}$ with a median of approximately $200\,m^2\,s^{-2}$ for NOCM, and in the 0–$375\,m^2\,s^{-2}$ range and approximate median of $125\,m^2\,s^{-2}$ for steady-state supercells (AD05, their Fig. 23). While there is overlap between these modes, the general trend is environments that produce supercells exhibiting OCM have comparatively lower SRH01 values compared to those exhibiting NOCM, which have the highest SRH01 values. Additionally, steady-state supercells have SRH01 values that are in between those of OCM and NOCM. The SRH01 for a particular storm provides information on the relative strength of the storm's inflow. Higher values of SRH01 are associated with a stronger near-ground, upward-directed perturbation pressure gradient force, which acts to intensify the low-level mesocyclone (Brooks and Wilhelmson 1993; Peters et al. 2020). The stronger the upward-directed vertical pressure gradient force near the surface, the more air that is drawn into the low-level mesocyclone, thus enhancing the storm's inflow. When SRH01 is low, the storm's inflow is expected to be relatively weak, and the opposite is true when SRH01 is high.

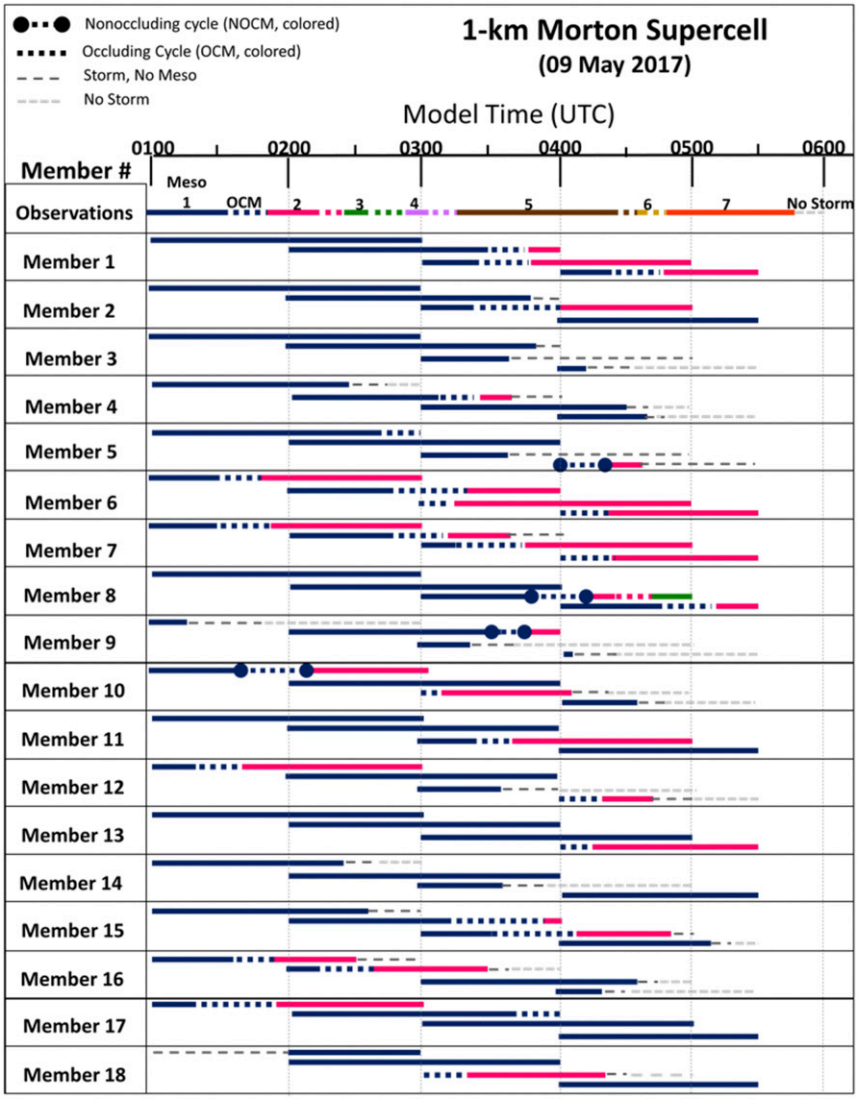

FIG. 10. Summary of results from 1-km, 18-member forecasts for the Morton supercell of 9 May 2017. WSR-88D radar observations are shown at the top with the results from each ensemble member below. For the ensemble members, there were four forecasts (0000, 0100, 0200, and 0300 UTC) analyzed and are displayed as stacked bars. Recall that the first hour is ignored, so if the forecast was initialized at 0000 UTC the bar begins at 0100 UTC.

Recall, many previous studies have identified a relationship between the balance of the supercell's inflow and outflow air and cycling frequency (Dowell and Bluestein 2002b,a; Beck et al. 2006; French et al. 2008). When the two are in balance, the supercell will generally be steady-state or cycle very infrequently. When the inflow and outflow are imbalanced, the mesocyclones are shed quickly, and these storms tend to cycle more frequently. Keeping this balance in mind, we will use SRH01 to examine the relative strength of the supercell's inflow. After analyzing inflow strength, the strength of the outflow will be examined to compare the relative inflow/outflow balance across the three cases and test if variations are consistent with the forecasted cycling frequencies.

The forecasted Elk City hodographs have the highest predicted SRH01 values, reaching approximately 489 $m^2 s^{-2}$ during its last forecast (Fig. 14). The enhancement of SRH01 in the Elk City supercell's environment by the LLJ can be seen in the evolution across different forecast times (Fig. 15). The environment in the 20 UTC forecast has comparatively low SRH01 values, but as the LLJ modifies the environment the later forecasts increase rapidly in SRH01. The high values of SRH01 for the Elk City supercell indicate that this storm has the potential to produce a strong mesocyclone and corresponding strong inflow.

In WoFS, the Hennessey supercell had the highest cycling frequency of 0.28 cycles per hour and produced all OCM

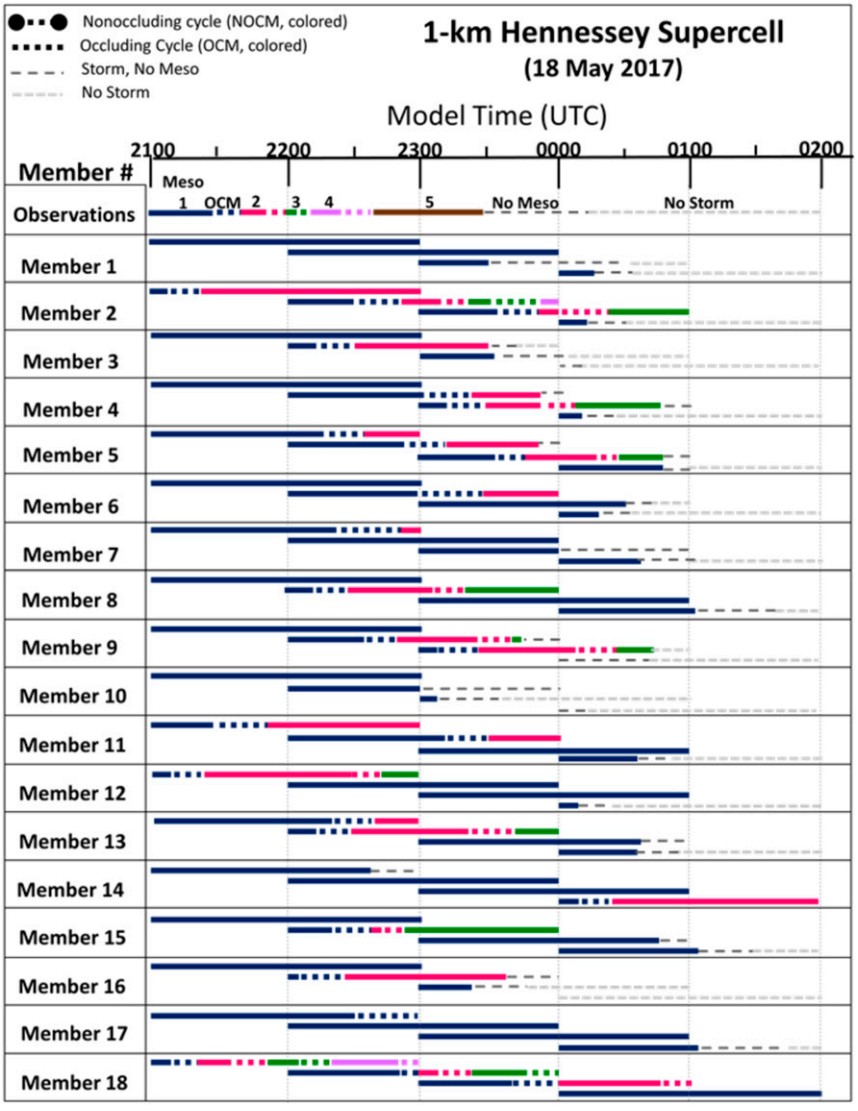

FIG. 11. As in Fig. 10, but for the Hennessey supercell of 18 May 2017. The 1-km forecasts are at 2000, 2100, 2200, and 2300 UTC.

cycles. The composite hodographs for this storm have the lowest SRH01 values in the far-inflow region of the storm (Fig. 14), as well as the lowest comparative values across the inflow sector (Fig. 15). These relatively low values of SRH01 compared to the other cases suggest lower potential for an intense mesocyclone and strong inflow winds. The forecasted hodographs also show possible modification from the LLJ, as the curvature and SRH01 magnitudes increase with forecast time (Fig. 14). The LLJ modification is also evident in the SRH01 values broken down by the forecast time (Fig. 15). Although the SRH01 values are still lower than all three storms, the field is still expanding and increasing as the LLJ influences the later forecast times.

Last, the forecasted hodographs for the Morton supercell have relatively high SRH01 values compared to the Hennessey supercell, but they are still slightly lower than the maximum values for Elk City (Fig. 14). The forecasts for this storm (0000–0300 UTC) occurred after the development of the LLJ, which may be why SRH01 is consistently around $400\,m^2\,s^{-2}$ for this storm (Fig. 14) and the SRH01 field stays relatively constant with time (Fig. 15). Based off the higher SRH01 values for this storm, one would expect the potential for stronger storm inflow, similar to the Elk City supercell.

Inferring the strength of a supercell's inflow using SRH01 alone does not give the full picture of its potential effect on cyclic mesocyclogenesis. One must also know the strength of the supercell's RFD outflow to understand the balance between the two flows. To measure the potential strength of each supercell's outflow, we examine the environmental potential for evaporative cooling by examining the height of the lifting condensation level (LCL). Lower LCL heights tend to be associated with suppressed evaporation that can lead to

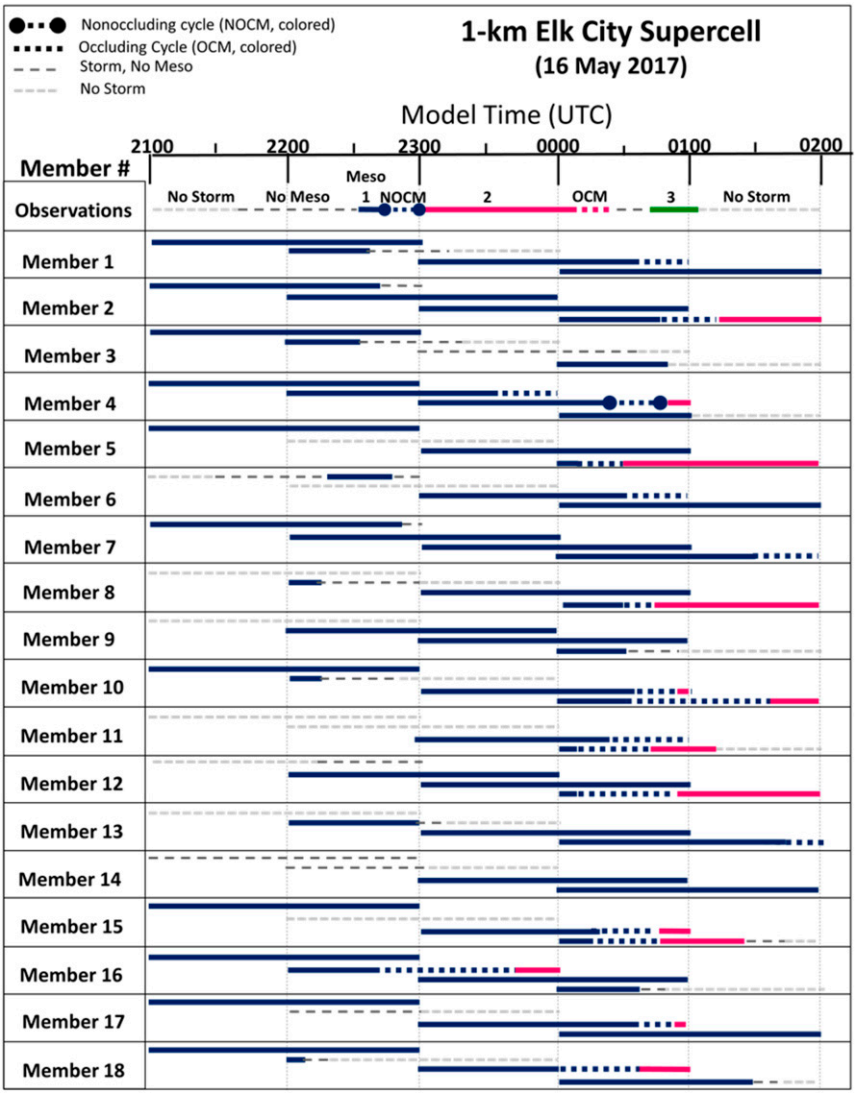

FIG. 12. As in Fig. 10, but for the Elk City supercell of 16 May 2017. The 1-km forecasts are at 2000, 2100, 2200, and 2300 UTC.

warmer cold pools (Markowski et al. 2002; Thompson et al. 2003; Markowski and Richardson 2014) and weaker outflow, whereas, higher LCL heights are indicative of enhanced evaporation, which may promote colder cold pools and stronger RFDs.

Therefore, to examine the potential strength of each supercell's outflow, we composite WoFS LCL height (Fig. 16b). The highest LCL heights (greater than 1400 m) were associated with the Hennessey supercell, whereas the lowest heights (approximately 600–800 m) occurred with the Morton supercell. This time, the Elk City supercell was the intermediate case with LCL heights around 1000 m. Assuming LCL height influences the relative strength of a supercell's outflow, the Hennessey storm would be expected to have the strongest outflow, with Elk City being next, and Morton having the weakest. This expectation is confirmed in composites of the low-level cold pools of each storm, where Morton has the smallest and weakest cold pool (0.8-K deficits) and Hennessey has an extensive, strong cold pool (approximately −2.4 K or lower; Fig. 16d).

Comparing the relative strength of the inflow for the Morton and Hennessey supercells to their outflow strength, the two would be considered out of balance. For instance, the Morton storm has relatively strong inflow and the weakest outflow. Hennessey has the strongest outflow and the weakest inflow. The imbalance between these storms' inflow and outflow strengths aligns with WoFS predictions of more cycling episodes for these two storms. Conversely, the Elk City supercell had strong inflow and moderate outflow. Compared to the other two storms, the Elk City supercell was more balanced between its inflow and outflow, which is consistent with the slower cycling frequency predicted by WoFS.

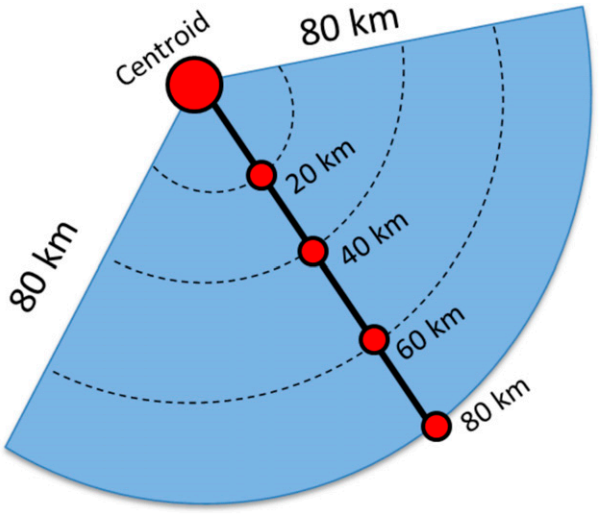

FIG. 13. Illustration of where in the inflow sector the hodographs are sampled every 20 km from the object's centroid (red dots). The centroid dot indicates the centroid of the supercell's mesocyclone object that was identified.

The balance between a supercell's inflow and outflow strength and its effect on cycling frequency is also related to that supercell's potential for tornadogenesis. If the outflow and inflow are imbalanced, then the low-level mesocyclones are swept quickly away from the updraft and the associated area of rich vorticity generation and potentially strong upward vertical acceleration. Thus, tornadogenesis and maintenance are often hindered for frequently cycling storms (e.g., Beck et al. 2006; French et al. 2008). However, if the flows are balanced then the low-level mesocyclone can remain under the updraft and in the area favorable for vertical vorticity generation (Dowell and Bluestein 2002a,b). This balance is associated with infrequently cycling or steady state supercells, in which there is a higher potential for these supercells to produce strong, long-lived tornadoes.

To further illustrate the relationship between cycling frequency and tornado potential, composites of significant tornado parameter (STP; Thompson et al. 2003, 2012) were created (Fig. 16c). The values of STP seem to vary inversely with each supercell's cycling frequency. The higher the cycling frequency of the supercell, such as with the Hennessey storm, the lower the STP values (Fig. 16c) and the lower potential for tornadoes, which in this case reflected observations as the Hennessey storm was nontornadic. Conversely, higher values of STP are associated with infrequently cycling supercells or supercells that are more steady-state in nature. For instance, the Elk City supercell has the highest STP values and the lowest cycling frequency. Those high STP values agree with the fact that this supercell produced many tornadoes, some very strong and destructive. Morton is, once again, a middle-ground case but that corresponds to the supercell producing two weak tornadoes and having a higher cycling frequency than the Elk City storm.

Out of all the environmental parameters composited for these three cases, STP appears to be the best correlated with a supercell's cycling frequency. As STP increases for a given storm, the cycling frequency decreases (i.e., they are inversely correlated). Therefore, the greater the chance of the supercell producing multiple tornadoes, the lower the potential that the storm may undergo frequent cyclic mesocyclogenesis. SRH01 and LCL height are important for determining the balance between inflow and outflow, but they have to be interpreted together to provide a complete picture of the potential cycling frequency. The calculation of STP takes into account the effective SRH, mixed-layer convective available potential energy (MLCAPE), mixed-layer convective inhibition (MLCIN), LCL height, and effective layer bulk shear (Thompson et al. 2012). However, WoFS uses 0–1-km SRH rather than effective SRH for the calculation of STP.

STP is already widely used for forecasting tornadoes. This research suggests another use for STP could be predicting the cycling frequency of supercells for a given day, which provides guidance on the potential for tornadogenesis. However, the relationship between STP and cycling frequency is a causality dilemma. Is the potential for tornadogenesis lower with low STP values because the supercell is rapidly cycling, or is it attributable to poor environmental conditions? Furthermore, is a higher cycling frequency a consequence of suboptimal tornado environments that are associated with lower STP? While the answer to this problem is outside the scope of this research, more cases could be analyzed in the future to examine the connection between STP, cycling frequency, and tornadogenesis.

4. Summary and conclusions

The purpose of this study was to test the capability of a short-term (0–3 h), storm-scale ensemble system (WoFS) to resolve and predict cyclic mesocyclogenesis, assess whether this process is physically representative of the current understanding for cyclic supercells, and if it can be used to potentially forecast the presence and frequency of cycling. Three cyclic supercells from May 2017 were chosen to examine how WoFS resolved and predicted cycling. Radar reflectivity and radial velocities from WSR-88D data were analyzed to create an observational database for each of the supercells to compare to the WoFS forecasts.

The default WoFS horizontal grid spacing of 3 km was changed to 1 km to compare results of cyclic mesocyclogenesis to that seen in AD02. Although the AD02 study suggested that cycling would not be observed at horizontal grid spacings of 3 km, WoFS did produce a few clear cases of cyclic-like processes at 3 km (Fig. 7). As expected, when the grid spacing was changed to 1 km, cycling became more frequent. The frequently cycling supercells in observations tended to have more forecasted cycles in WoFS. For instance, the Hennessey and Morton supercells cycled frequently in observations, producing a total of four and six identified cycles, respectively. For the Hennessey supercell, WoFS forecasted a total of 42 cycles, with a mean cycling frequency of 0.28 cycles per hour. Morton had a slightly lower number of cycles and cycling frequency at 32 cycles and 0.22 cycles per hour, respectively. However, the Elk City supercell cycled infrequently in observations with only two periods of cycling. In turn, WoFS only

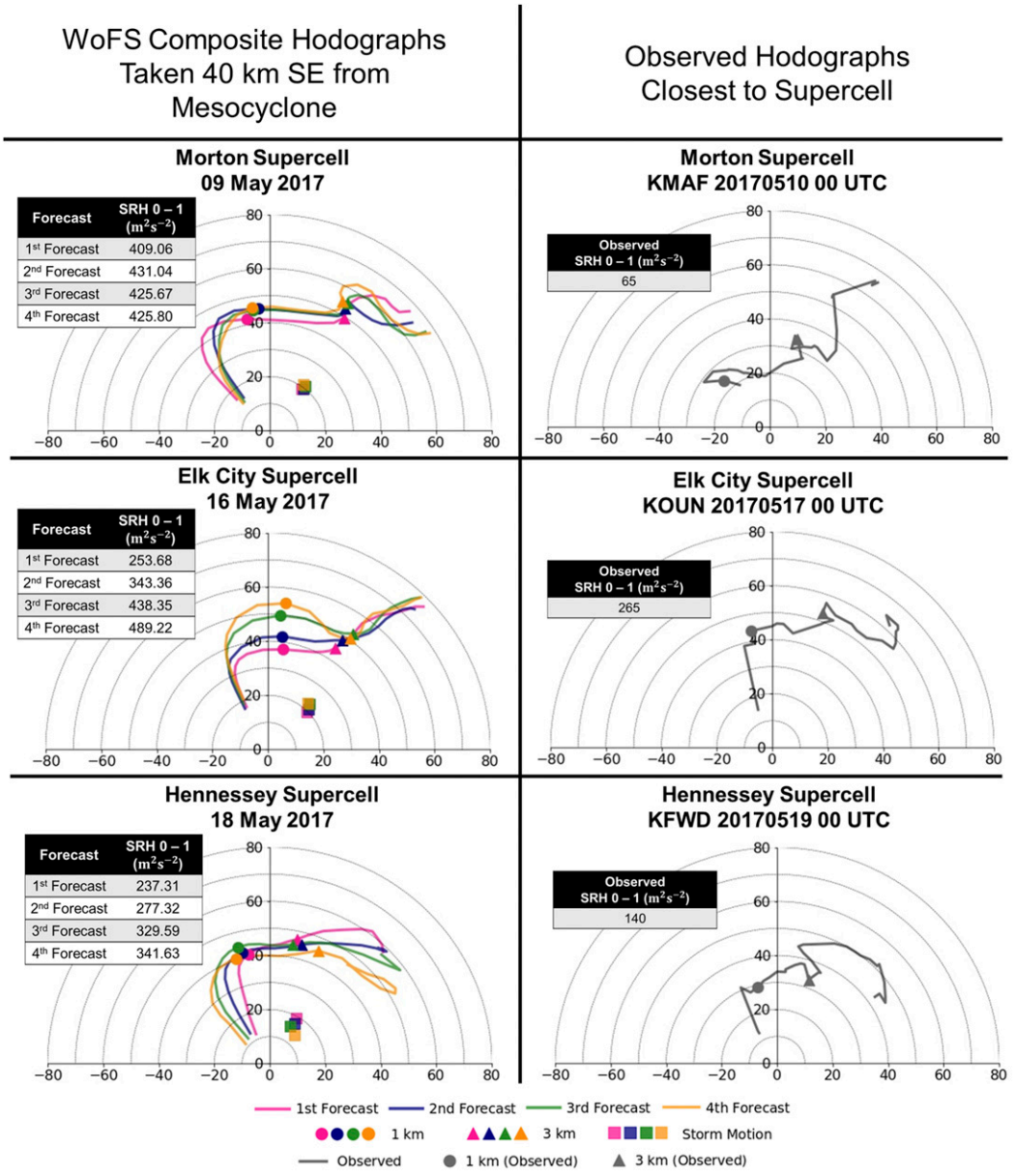

FIG. 14. Comparison of the WoFS composite hodographs to the observed hodographs closest to each supercell. The circles and triangles (color coded by forecast) denote where the 1- and 3-km heights are on the hodographs, respectively. The squares denote the storm motion vector. Wind speed is in knots (kt; 1 kt $\approx$ 0.51 m s^{-1}). The observed hodographs for the Morton and Hennessey supercells are relatively far away due to data issues at the closer stations. However, these are just used as a check of the environmental conditions for each day.

forecasted a total of 19 cycles for this storm with a cycling frequency of 0.13 cycles per hour. WoFS underpredicted the cycling frequencies compared to observations, but the fact that it differentiated between frequently and infrequently cycling storms shows promise.

Analysis of the 1-km forecasts suggest WoFS can potentially provide guidance of supercell cycling frequency. To examine the differences in WoFS's forecasted frequencies, composites of the inflow environments of the three supercells were created to intercompare bulk differences between their respective mesoscale environments, and compare those results to AD05. The WoFS hodographs were mostly quarter-circle shaped with shear being concentrated in the lowest 1 km (Fig. 14). According to AD05 (their Fig. 23), the WoFS hodographs would fall into the NOCM category, while the prominent mode of cycles predicted by WoFS was OCM. However, the full-physics WoFS simulations are configured differently than

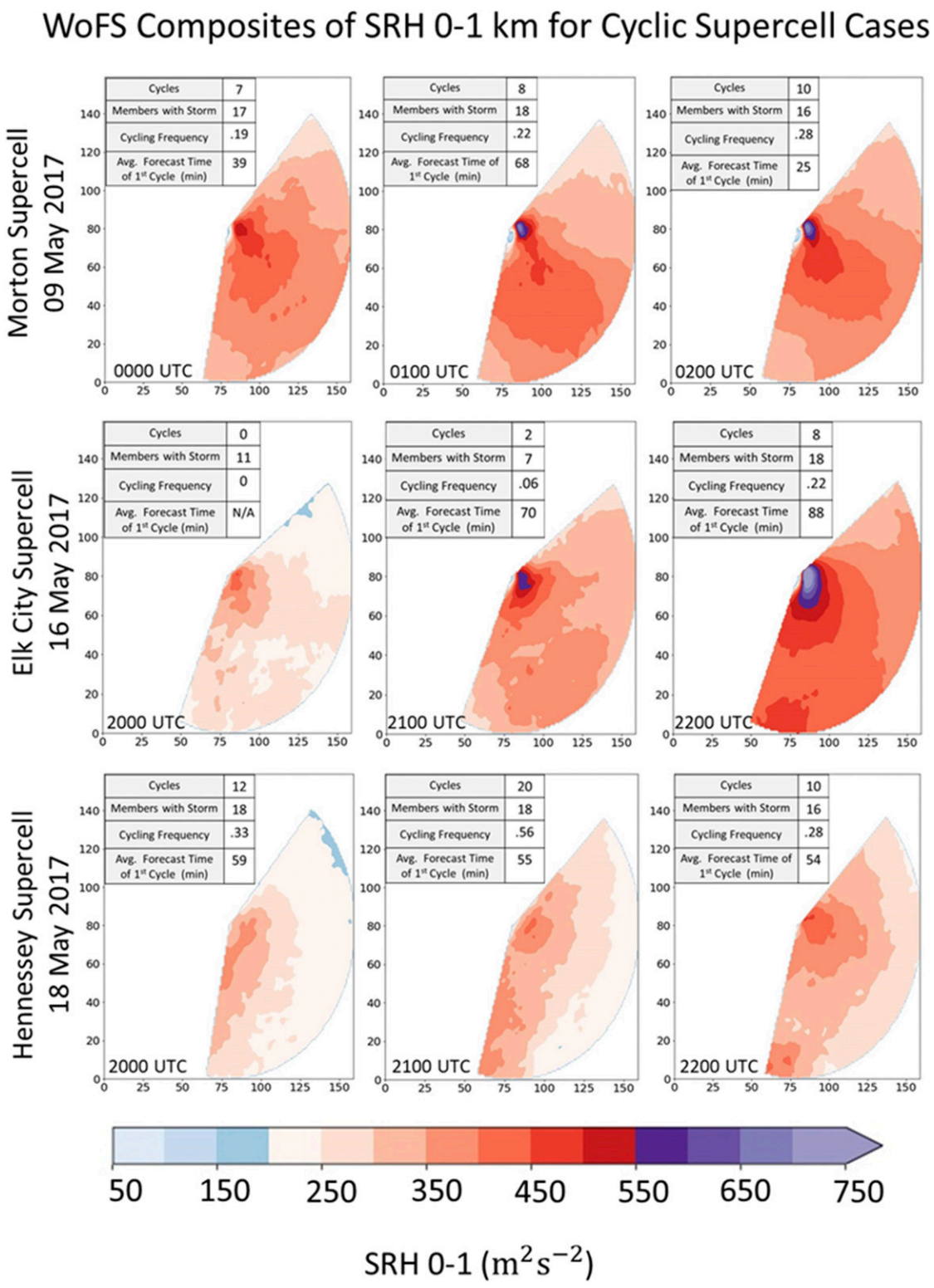

FIG. 15. Individual WoFS forecast SRH 0–1-km composites for the three supercells. Only, the first three forecasts (labeled in the bottom-left corner) composites are shown. The tables in the upper-right corner help to annotate how many cycles were observed in that forecast, the number of members with the supercell present (out of 18), the cycling frequency (cycles per hour), and the average forecast time of the first cycle (minutes into the forecast; excluding the first hour).

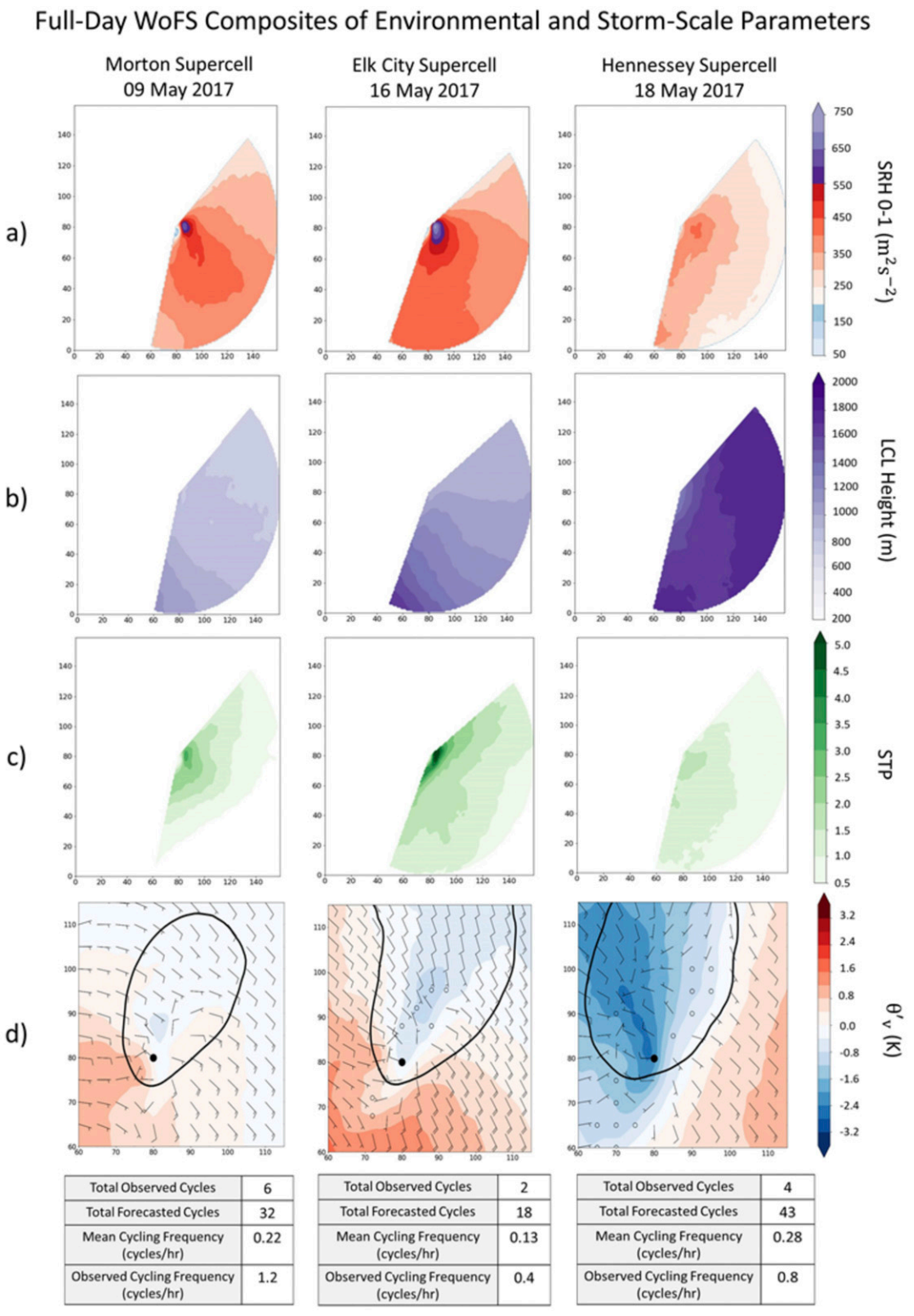

FIG. 16. Full-day inflow sector composites for (a) SRH 0–1 km, (b) LCL height, (c) STP, and (d) perturbation potential temperature with surface-based winds (barbs) and the 30-dBZ reflectivity line (black contour). The black dot in (d) represents the composite centroid point, which corresponds to the average mesocyclone location. Additional information about the case days are given in the charts below: total observed cycles, total forecasted cycles, average observed cycling frequency, and forecasted cycling frequency.

the idealized simulations ran by AD05, which is known to produce differences in cycling character (AD02).

Although the shape of the supercells' hodographs were not consistent with the predominant cycling modes found by AD05, our studies were similar in that the inflow environment was having an impact on the cycling frequencies for these storms. First, composites of SRH01 were analyzed to understand the relative strength of each supercell's inflow (Figs. 15 and 16a). Next, examination of LCL height composites (Fig. 16b) helped to understand the strength of each supercell's cold pool (Fig. 16d) and associated RFD outflow. Coupling SRH01 and LCL height allowed for the analysis of whether each storm's inflow and outflow were balanced or not, which has been shown to influence the cycling frequency in past supercells (Dowell and Bluestein 2002a,b; Beck et al. 2006; French et al. 2008). The Hennessey and Morton supercells were the most imbalanced, as the Hennessey supercell was outflow dominant and the Morton supercell was inflow dominant. These imbalances corresponded with higher cycling frequencies for both storms. However, Elk City's inflow and outflow were more balanced and corresponded to it having the lowest predicted and observed cycling frequency.

The balance between a storm's inflow and outflow and how it affects cycling frequency is also related to that storm's potential for tornadogenesis. If the flows are imbalanced, the mesocyclones are shed more quickly, and the potential for tornadogenesis is reduced. Consequently, supercells that cycle frequently often have a lower potential for producing tornadoes (Beck et al. 2006; French et al. 2008). STP was composited to examine the relationship between cycling frequency and tornadogenesis (Fig. 16c). The frequently cycling supercells (Hennessey and Morton) tended to have lower STP values compared to the Elk City supercell that had the highest STP values and lowest cycling frequency. STP was inversely correlated with cycling frequency for this dataset. This result provides a proof of concept that accurately forecasting cycling frequency may provide useful guidance on tornado potential.

Even though, in the cases examined, WoFS did not accurately predict the timing of the cycles compared to observations, it still showed potential in forecasting the presence and cycling frequency of supercells. From a predictability standpoint, WoFS run with a sufficiently small grid spacing may provide forecasters with situational awareness on the presence and cycling frequency of cyclic supercells on a given day. Also, knowing WoFS can resolve smaller-scale processes such as cyclic mesocyclogenesis shows promise for being able to skillfully forecast the processes leading to tornadogenesis, which is a long-term goal of WoF (Stensrud et al. 2009, 2013). Until then, there are some parallels between cycling frequency and tornado potential. STP is a widespread forecasting metric for predicting tornadoes, but it also seems to be useful in predicting the cycling frequency of supercells. Tornado potential increases (decreases) with increasing (decreasing) STP, but the associated cycling frequency of the supercell decreases (increases). However, the relationship between cycling frequency and STP remains a causality dilemma. It is difficult to decipher if tornado potential is lower with low values of STP because cycling frequency is higher, or because of poor environmental conditions. To better understand this relationship, more supercell cases should be analyzed in the future.

A limitation of this study is the small dataset considered. To more comprehensively understand WoFS's forecasting potential for cyclic supercells and usability for determining tornado potential for forecasters, more supercell cases need to be examined. Additionally, there needs to be more observational studies on the impacts of different inflow environmental parameters on cycling frequency. These observations could also be compared to our inflow sector composites to see if WoFS is accurately predicting the environment around these storms. Another topic for future work consists of examining the influence of cell mergers on cycling. Mergers can affect the intensity of storm outflow (Hastings and Richardson 2016), which may also trigger cyclic mesocyclogenesis to occur. Therefore, different types of cell mergers may either suppress of enhance cycling depending on the dynamics at work.

The larger goal of this research was to provide some insight in the advantages of running WoFS at a 1-km grid spacing. If updated to a finer grid spacing, WoFS may have the potential to predict the presence and cycling frequency of supercells on a given day, thus, aiding forecasters in determining the possibility for tornadogenesis.

Acknowledgments. Funding for this research was provided by NOAA/Office of Oceanic and Atmospheric Research under NOAA–University of Oklahoma Cooperative Agreement NA 11OAR4320072, under the U.S. Department of Commerce with additional funding from the Warn-on-Forecast project. The authors appreciate the feedback provided by Drs. Steven Cavallo and Xuguang Wang on early versions of this work. We also thank Monte Flora for his work on the object identification code, as well as the three anonymous reviewers for providing feedback. All analyses and visualizations were produced using the freely provided Anaconda Python distribution (v.2.7) and the SciPy, Matplotlib, netcdf4, numpy, scikit-image, and scikit-learn libraries.

Data availability statement. All WoFS data used by this study are freely available at https://data.nssl.noaa.gov/thredds/catalog/PARR/2020/Kelsey-Britt.html and WSR-88D data are available through NOAA via the National Centers for Environmental Information (NCEI).

REFERENCES

Adlerman, E. J., and K. K. Droegemeier, 2002: The sensitivity of numerically simulated cyclic mesocyclogenesis to variations in model physical and computational parameters. *Mon. Wea. Rev.*, **130**, 2671–2691, https://doi.org/10.1175/1520-0493(2002)130<2671:TSONSC>2.0.CO;2.

——, and ——, 2005: The dependence of numerically simulated cyclic mesocyclogenesis upon environmental vertical wind shear. *Mon. Wea. Rev.*, **133**, 3595–3623, https://doi.org/10.1175/MWR3039.1.

——, ——, and R. Davies-Jones, 1999: A numerical simulation of cyclic mesocyclogenesis. *J. Atmos. Sci.*, **56**, 2045–2069, https://doi.org/10.1175/1520-0469(1999)056<2045:ANSOCM>2.0.CO;2.

Anderson, J. L., and N. Collins, 2007: Scalable implementations of ensemble filter algorithms for data assimilation. *J. Atmos.*

Oceanic Technol., **24**, 1452–1463, https://doi.org/10.1175/JTECH2049.1.

——, T. Hoar, K. Raeder, H. Liu, N. Collins, R. Torn, and A. Avellano, 2009: The Data Assimilation Research Testbed: A community facility. *Bull. Amer. Meteor. Soc.*, **90**, 1283–1296, https://doi.org/10.1175/2009BAMS2618.1.

Beck, J. R., J. L. Schroeder, and J. M. Wurman, 2006: High-resolution dual-Doppler analyses of the 29 May 2001 Kress, Texas, cyclic supercell. *Mon. Wea. Rev.*, **134**, 3125–3148, https://doi.org/10.1175/MWR3246.1.

Bluestein, H. B., 2009: The formation and early evolution of the Greensburg, Kansas, tornadic supercell on 4 May 2007. *Wea. Forecasting*, **24**, 899–920, https://doi.org/10.1175/2009WAF2222206.1.

Brooks, H. E., and R. B. Wilhelmson, 1993: Hodograph curvature and updraft intensity in numerically modeled supercells. *J. Atmos. Sci.*, **50**, 1824–1833, https://doi.org/10.1175/1520-0469(1993)050<1824:HCAUII>2.0.CO;2.

Bunkers, M. J., B. A. Klimowski, J. W. Zeitler, R. L. Thompson, and M. L. Weisman, 2000: Predicting supercell motion using a new hodograph technique. *Wea. Forecasting*, **15**, 61–79, https://doi.org/10.1175/1520-0434(2000)015<0061:PSMUAN>2.0.CO;2.

Burgess, D. W., V. T. Wood, and R. A. Brown, 1982: Mesocyclone evolution statistics. Preprints, *12th Conf. on Severe Local Storms*, San Antonio, TX, Amer. Meteor. Soc., 422–424.

Darkow, G. L., and J. C. Roos, 1970: Multiple tornado producing thunderstorms and their apparent cyclic variations in intensity. *14th Conf. on Radar Meteorology*, Tucson, AZ, Amer. Meteor. Soc., 305–308.

Dawson, D. T., II, L. J. Wicker, E. R. Mansell, and R. L. Tanamachi, 2012: Impact of the environmental low-level wind profile on ensemble forecasts of the 4 May 2007 Greensburg, Kansas, tornadic storm and associated mesocyclones. *Mon. Wea. Rev.*, **140**, 696–716, https://doi.org/10.1175/MWR-D-11-00008.1.

Dowell, D. C., and H. B. Bluestein, 2002a: The 8 June 1995 McLean, Texas, storm. Part I: Observations of cyclic tornadogenesis. *Mon. Wea. Rev.*, **130**, 2626–2648, https://doi.org/10.1175/1520-0493(2002)130<2626:TJMTSP>2.0.CO;2.

——, and ——, 2002b: The 8 June 1995 McLean, Texas, storm. Part II: Cyclic tornado formation, maintenance, and dissipation. *Mon. Wea. Rev.*, **130**, 2649–2670, https://doi.org/10.1175/1520-0493(2002)130<2649:TJMTSP>2.0.CO;2.

——, and Coauthors, 2016: Development of a High-Resolution Rapid Refresh Ensemble (HRRRE) for severe weather forecasting. *28th Conf. on Severe Local Storms*, Portland, OR, Amer. Meteor. Soc., 8B.2, https://ams.confex.com/ams/28SLS/webprogram/Paper301555.html.

Flora, M. L., P. S. Skinner, C. K. Potvin, A. E. Reinhart, T. A. Jones, N. Yussouf, and K. H. Knopfmeier, 2019: Object-based verification of short-term, storm-scale probabilistic mesocyclone guidance from an experimental warn-on-forecast system. *Wea. Forecasting*, **34**, 1721–1739, https://doi.org/10.1175/WAF-D-19-0094.1.

French, M. M., H. B. Bluestein, D. C. Dowell, L. J. Wicker, M. R. Kramar, and A. L. Pazmany, 2008: High-resolution, mobile Doppler radar observations of cyclic mesocyclogenesis in a supercell. *Mon. Wea. Rev.*, **136**, 4997–5016, https://doi.org/10.1175/2008MWR2407.1.

——, ——, I. PopStefanija, C. A. Baldi, and R. T. Bluth, 2013: Reexamining the vertical development of tornadic vortex signatures in supercells. *Mon. Wea. Rev.*, **141**, 4576–4601, https://doi.org/10.1175/MWR-D-12-00315.1.

Hastings, R., and Y. Richardson, 2016: Long-term morphological changes in simulated supercells following mergers with nascent supercells in directionally varying shear. *Mon. Wea. Rev.*, **144**, 471–499, https://doi.org/10.1175/MWR-D-15-0193.1.

Heinselman, P. L., and S. M. Torres, 2011: High-temporal-resolution capabilities of the National Weather Radar Testbed Phased-Array radar. *J. Appl. Meteor. Climatol.*, **50**, 579–593, https://doi.org/10.1175/2010JAMC2588.1.

——, D. L. Priegnitz, K. L. Manross, T. M. Smith, and R. W. Adams, 2008: Rapid sampling of severe storms by the National Weather Radar Testbed Phased Array radar. *Wea. Forecasting*, **23**, 808–824, https://doi.org/10.1175/2008WAF2007071.1.

Houser, J. L., H. B. Bluestein, and J. C. Snyder, 2015: Rapid-scan, polarimetric, Doppler radar observations of tornadogenesis and tornado dissipation in a tornadic supercell: The "El Reno, Oklahoma" storm of 24 May 2011. *Mon. Wea. Rev.*, **143**, 2685–2710, https://doi.org/10.1175/MWR-D-14-00253.1.

Jones, T. A., K. Knopfmeier, D. Wheatley, G. Creager, P. Minnis, and R. Palikonda, 2016: Storm-scale data assimilation and ensemble forecasting with the NSSL Experimental Warn-on-Forecast system. Part II: Combined radar and satellite data experiments. *Wea. Forecasting*, **31**, 297–327, https://doi.org/10.1175/WAF-D-15-0107.1.

Kumjian, M. R., A. V. Ryzhkov, V. M. Melnikov, and T. J. Schuur, 2010: Rapid-scan super-resolution observations of a cyclic supercell with a dual-polarization WSR-88D. *Mon. Wea. Rev.*, **138**, 3762–3786, https://doi.org/10.1175/2010MWR3322.1.

Labriola, J., N. Snook, Y. Jung, B. Putnam, and M. Xue, 2017: Ensemble hail prediction for the storms of 10 May 2010 in south-central Oklahoma using single- and double-moment microphysical schemes. *Mon. Wea. Rev.*, **145**, 4911–4936, https://doi.org/10.1175/MWR-D-17-0039.1.

Lemon, L. R., and C. A. Doswell, 1979: Severe thunderstorm evolution and mesocyclone structure as related to tornadogenesis. *Mon. Wea. Rev.*, **107**, 1184–1197, https://doi.org/10.1175/1520-0493(1979)107<1184:STEAMS>2.0.CO;2.

Mansell, E. R., C. L. Ziegler, and E. C. Bruning, 2010: Simulated electrification of a small thunderstorm with two-moment bulk microphysics. *J. Atmos. Sci.*, **67**, 171–194, https://doi.org/10.1175/2009JAS2965.1.

Markowski, P. M., and Y. P. Richardson, 2014: The influence of environmental low-level shear and cold pools on tornadogenesis: Insights from idealized simulations. *J. Atmos. Sci.*, **71**, 243–275, https://doi.org/10.1175/JAS-D-13-0159.1.

——, J. M. Straka, and E. N. Rasmussen, 2002: Direct surface thermodynamic observations within the rear-flank downdrafts of nontornadic and tornadic supercells. *Mon. Wea. Rev.*, **130**, 1692–1721, https://doi.org/10.1175/1520-0493(2002)130<1692:DSTOWT>2.0.CO;2.

Mead, C., and R. Thompson, 2011: Environmental characteristics associated with nocturnal significant-tornado events in the Great Plains. *Electron. J. Severe Storms Meteor.*, **6** (6), http://www.ejssm.org/ojs/index.php/ejssm/article/viewArticle/84.

Parker, M. D., 2014: Composite VORTEX2 supercell environments from near-storm soundings. *Mon. Wea. Rev.*, **142**, 508–529, https://doi.org/10.1175/MWR-D-13-00167.1.

Peters, J. M., C. J. Nowotarski, J. P. Mulholland, and R. L. Thompson, 2020: The influences of effective inflow layer streamwise vorticity and storm-relative flow on supercell updraft properties. *J. Atmos. Sci.*, **77**, 3033–3057, https://doi.org/10.1175/JAS-D-19-0355.1.

Potvin, C. K., and L. J. Wicker, 2013: Assessing ensemble forecasts of low-level supercell rotation within an OSSE framework. *Wea. Forecasting*, **28**, 940–960, https://doi.org/10.1175/WAF-D-12-00122.1.

Powers, J. G., and Coauthors, 2017: The Weather Research and Forecasting Model: Overview, system efforts, and future directions. *Bull. Amer. Meteor. Soc.*, **98**, 1717–1737, https://doi.org/10.1175/BAMS-D-15-00308.1.

Skamarock, W. C., 2004: Evaluating mesoscale NWP models using kinetic energy spectra. *Mon. Wea. Rev.*, **132**, 3019–3032, https://doi.org/10.1175/MWR2830.1.

——, and Coauthors, 2008: A description of the Advanced Research WRF version 3. NCAR Tech. Note NCAR/TN-475+STR, 113 pp., https://doi.org/10.5065/D68S4MVH.

Skinner, P. S., L. J. Wicker, D. M. Wheatley, and K. H. Knopfmeier, 2016: Application of two spatial verification methods to ensemble forecasts of low-level rotation. *Wea. Forecasting*, **31**, 713–735, https://doi.org/10.1175/WAF-D-15-0129.1.

——, and Coauthors, 2018: Object-based verification of a prototype Warn-on-Forecast system. *Wea. Forecasting*, **33**, 1225–1250, https://doi.org/10.1175/WAF-D-18-0020.1.

Smith, B. T., R. L. Thompson, J. S. Grams, C. Broyles, and H. E. Brooks, 2012: Convective modes for significant severe thunderstorms in the contiguous United States. Part I: Storm classification and climatology. *Wea. Forecasting*, **27**, 1114–1135, https://doi.org/10.1175/WAF-D-11-00115.1.

——, T. E. Castellanos, A. C. Winters, C. M. Mead, A. R. Dean, and R. L. Thompson, 2013: Measured severe convective wind climatology and associated convective modes of thunderstorms in the contiguous United States, 2003–09. *Wea. Forecasting*, **28**, 229–236, https://doi.org/10.1175/WAF-D-12-00096.1.

——, R. L. Thompson, A. R. Dean, and P. T. Marsh, 2015: Diagnosing the conditional probability of tornado damage rating using environmental and radar attributes. *Wea. Forecasting*, **30**, 914–932, https://doi.org/10.1175/WAF-D-14-00122.1.

Snook, N., Y. Jung, J. Brotzge, B. Putnam, and M. Xue, 2016: Prediction and ensemble forecast verification of hail in the supercell storms of 20 May 2013. *Wea. Forecasting*, **31**, 811–825, https://doi.org/10.1175/WAF-D-15-0152.1.

Stensrud, D. J., and Coauthors, 2009: Convective-scale Warn-on-Forecast system: A vision for 2020. *Bull. Amer. Meteor. Soc.*, **90**, 1487–1500, https://doi.org/10.1175/2009BAMS2795.1.

——, and Coauthors, 2013: Progress and challenges with Warn-on-Forecast. *Atmos. Res.*, **123**, 2–16, https://doi.org/10.1016/j.atmosres.2012.04.004.

Thompson, R. L., R. Edwards, J. A. Hart, K. L. Elmore, and P. Markowski, 2003: Close proximity soundings within supercell environments obtained from the Rapid Update Cycle. *Wea. Forecasting*, **18**, 1243–1261, https://doi.org/10.1175/1520-0434(2003)018<1243:CPSWSE>2.0.CO;2.

——, B. T. Smith, J. S. Grams, A. R. Dean, and C. Broyles, 2012: Convective modes for significant severe thunderstorms in the contiguous United States. Part II: Supercell and QLCS tornado environments. *Wea. Forecasting*, **27**, 1136–1154, https://doi.org/10.1175/WAF-D-11-00116.1.

——, and Coauthors, 2017: Tornado damage rating probabilities derived from WSR-88D data. *Wea. Forecasting*, **32**, 1509–1528, https://doi.org/10.1175/WAF-D-17-0004.1.

Wheatley, D. M., K. H. Knopfmeier, T. A. Jones, and G. J. Creager, 2015: Storm-scale data assimilation and ensemble forecasting with the NSSL experimental Warn-on-Forecast system. Part I: Radar data experiments. *Wea. Forecasting*, **30**, 1795–1817, https://doi.org/10.1175/WAF-D-15-0043.1.

Yussouf, N., E. R. Mansell, L. J. Wicker, D. M. Wheatley, and D. J. Stensrud, 2013: The ensemble Kalman filter analyses and forecasts of the 8 May 2003 Oklahoma city tornadic supercell storm using single- and double-moment microphysics schemes. *Mon. Wea. Rev.*, **141**, 3388–3412, https://doi.org/10.1175/MWR-D-12-00237.1.

——, D. C. Dowell, L. J. Wicker, K. H. Knopfmeier, and D. M. Wheatley, 2015: Storm-scale data assimilation and ensemble forecasts for the 27 April 2011 severe weather outbreak in Alabama. *Mon. Wea. Rev.*, **143**, 3044–3066, https://doi.org/10.1175/MWR-D-14-00268.1.

——, J. S. Kain, and A. J. Clark, 2016: Short-term probabilistic forecasts of the 31 May 2013 Oklahoma tornado and flash flood event using a continuous-update-cycle storm-scale ensemble system. *Wea. Forecasting*, **31**, 957–983, https://doi.org/10.1175/WAF-D-15-0160.1.